

The Momentum Kick Model Description of the Near-Side Ridge and Jet Quenching

Cheuk-Yin Wong

Physics Division, Oak Ridge National Laboratory, Oak Ridge, TN 37831*

(Dated: November 3, 2018)

In the momentum kick model, a near-side jet emerges near the surface, kicks medium partons, loses energy, and fragments into the trigger particle and fragmentation products. The kicked medium partons subsequently materialize as the observed ridge particles, which carry direct information on the magnitude of the momentum kick and the initial parton momentum distribution at the moment of jet-(medium parton) collisions. The initial parton momentum distribution extracted from the STAR ridge data for central AuAu collisions at $\sqrt{s_{NN}} = 200$ GeV has a thermal-like transverse momentum distribution and a rapidity plateau structure with a relatively flat distribution at mid-rapidity and sharp kinematic boundaries at large rapidities. Such a rapidity plateau structure may arise from particle production in flux tubes, as color charges and anti-color charges separate at high energies. The centrality dependence of the ridge yield and the degree of jet quenching can be consistently described by the momentum kick model.

PACS numbers: 25.75.Gz 25.75.Dw

I. INTRODUCTION

In central high-energy heavy-ion collisions, jets are produced in nucleon-nucleon collisions and they interact with the dense medium produced in the interacting region. Depending on the relative azimuthal angle relative to the trigger particle, observed high- p_t jets can be classified as near-side jets or away-side jets. An away-side jet is associated with a broad cone of particles pointing azimuthally opposite to the trigger particle direction. The strong attenuation of the away-side jet in its passage through the produced dense matter is one of the many notable experimental observations in relativistic heavy-ion collisions and is a signature for the production of the strongly-coupled quark-gluon plasma [1, 2, 3, 4].

On the other hand, a near-side jet is characterized by the presence of associated particles within a narrow azimuthal angle along the trigger particle direction. It retains many of the characteristics of the associated fragmentation products as those of a jet in pp and peripheral heavy-ion collisions. The near-side jet occurs when the high- p_t jet emerges near the surface of the produced parton medium.

Recently, the STAR Collaboration [5, 6, 7, 8, 9, 10, 11, 12, 13, 14, 15] observed a $\Delta\phi$ - $\Delta\eta$ correlation of particles associated with a near-side, high- p_t trigger particle in central AuAu collisions at $\sqrt{s_{NN}} = 200$ GeV at RHIC, where $\Delta\phi$ and $\Delta\eta$ are the azimuthal angle and pseudorapidity differences measured relative to the trigger particle, respectively. Particles associated with the near-side jet can be decomposed into a “jet component”, corresponding to fragmentation products of the near-side jet at $(\Delta\phi, \Delta\eta) \sim (0, 0)$, and a “ridge component” at $\Delta\phi \sim 0$ with a ridge structure in $\Delta\eta$. Similar $\Delta\phi$ - $\Delta\eta$ correlations associated with a near-side jet have also been observed by the PHENIX Collaboration [16, 17] and the PHOBOS Collaboration [18]. While many theoretical models [19, 20, 21, 22, 23, 24, 25, 26, 27, 28, 29, 30, 31, 32, 33, 34, 35] have been proposed to discuss the jet structure and related phenomena, the ridge phenomenon has not yet been fully understood.

Previously, a momentum kick model was put forth to explain the ridge phenomenon [19, 20, 21]. The model assumes that a near-side jet occurs near the surface, kicks medium partons, loses energy along its way, and fragments into the trigger and its associated fragmentation products (the “jet component”) (Fig. 1). Those medium partons that are kicked by the jet acquire a momentum kick along the jet direction. They subsequently materialize by parton-hadron duality as ridge particles in the “ridge component” (Fig. 1). They carry direct information on the momentum distribution of the medium partons at the moment of jet-(medium parton) collisions, for which not much information has been obtained from direct experimental measurements. As the early state of the medium partons is an important physical quantity, it is therefore useful to examine the early parton momentum distribution using the momentum kick model.

A previous momentum kick model analysis gave theoretical results in qualitative agreement with experimental data [19]. We arrived at the interesting observation that at the moment of jet-(medium parton) collisions the parton transverse slope parameter T is slightly higher and the rapidity width substantially greater than corresponding quantities of their evolution products at the end-point of the nucleus-nucleus collision. We would like to refine the

* wongc@ornl.gov

model and give a quantitative comparison with experiment. We also wish to explore the early parton momentum distribution over a wider kinematic range of different transverse momenta and rapidities to search for interesting and novel features of the initial parton momentum distribution.

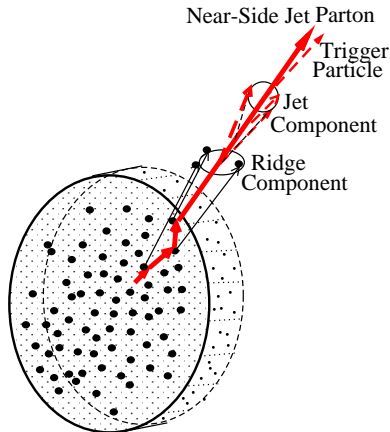


FIG. 1: (Color online) Schematic representation of the momentum kick model. A near-side jet parton (represented by adjoining thick arrows) occurs in a dense medium, whose partons are represented by solid circular points. The jet parton kicks many medium partons, loses energy, radiates, and fragments into the trigger particle and associated “jet component” particles. The medium partons that are kicked by the jet parton acquire a momentum kick along the jet direction and materialize as associated “ridge component” particles. Not shown in the figure is the away-side jet opposite to the near-side jet.

We shall show that the extracted early parton distribution has a plateau rapidity structure. Rapidity distributions in the form of a plateau have been known in QCD particle production processes both experimentally and theoretically. Experimental evidence for a plateau rapidity distributions along the sphericity axis or the thrust axis has been found in π^\pm production in e^+e^- annihilation [36, 37, 38, 39, 40, 41]. The rapidity distributions for K^\pm production also show a plateau structure with a depression in an extended region around $y \sim 0$. As a function of energy, the shape of the rapidity distribution for the sum of all particles produced in e^+e^- annihilation is a plateau with either a flat distribution or a small depression at $y \sim 0$ [40]. The width of the rapidity plateau increases as a function of increasing center-of mass energy.

Theoretically, the rapidity plateau structure has been known in many earlier investigations of particle production processes in QCD, when a quark pulls away from an anti-quark at high energies [42, 43, 44, 45, 46]. The theoretical basis in the work of Refs. [42, 43, 44, 45] comes from the approximate connection between QCD and QED2 [47, 48, 49, 50]. We would like to show more explicitly here how the transverse confinement in a flux tube allows one to establish an approximate connection between the field theories of QED2 and QCD in high energy processes. Using such a connection, we wish to review here how the rapidity plateau structure occurs when a color charge separates from an anti-color charge at high energies.

The early stage of the nucleus-nucleus collision comprise of many simultaneous elementary particle production processes involving a quark pulling away from an anti-quark (or qq diquark) at high energies. As elementary processes lead to plateau rapidity distributions, the rapidity distribution of the medium partons at the early stage of the nucleus-nucleus collision should retain the rapidity plateau characteristics.

The parton momentum distribution is only one aspect of the momentum kick model. The momentum loss of the jet in its passage through the medium is another important aspect. While many theoretical treatments of the jet quenching phenomenon have been presented previously [51], the investigation of the jet quenching phenomenon in connection with ridge particles associated with the jet will provide a different and complimentary perspective. The ridge yield and the quenching of the emerging jet will depend on the number of medium partons kicked by the jet along its way. A successful simultaneous description of the centrality dependence of the ridge yield and jet quenching will provide a consistent picture of the interaction between a jet and the medium. It will also pave the way for a future Monte Carlo implementation of the momentum kick model where many refinements and improvements can be included.

In this paper, we shall limit our attention to particles associated with the near-side jet. In the context of the present investigation, the ridge particle momentum distributions in nucleus-nucleus collisions refer implicitly to those measured on a “per jet trigger” basis, unless indicated otherwise. For brevity of terminology, the term “jet” will be used both for the parent “jet parton” that passes through the medium and also for the daughter “jet component” of associated particles. The ambiguity of the meaning of the term can be easily resolved by context.

This paper is organized as follows. In Section II we summarize the momentum kick model and relate the ridge yield to the number of kicked medium partons. In Section III, we give the relationship between the initial and final parton momentum distributions under the action of a momentum kick. In Section IV, we specify how the initial parton momentum distribution is parametrized. In order to determine the initial parton momentum distribution from the observed total particle distribution in central AuAu collisions, we parametrize in Section V the jet momentum distribution associated with the near-side jet in pp collisions. The momentum distribution of mid-rapidity associated particles in central AuAu collisions at $\sqrt{s_{NN}} = 200$ GeV are then analyzed in Section VI. In Section VII, we display explicitly the initial parton momentum distribution extracted from the ridge data. In Section VIII, we examine the connection between QCD and QED2 in the presence of transverse confinement and study the origin of the rapidity plateau when a color charge separates from an anti-color charge at high energies. In Section IX, the field theory of bosonized QED2 is then used to study particle production as an initial-value problem. The evolution of the medium parton momentum distribution is discussed in Section X. In Section XI, we turn our attention to the propagation of the jet and the dependence of the jet fragmentation function on the number of jet-(medium parton) collisions. In Section XII, the centrality dependence the ridge yield and jet quenching is examined. In Section XIII, we examine the dependence of the ridge yield on the energy and mass number of the colliding nuclei. In Section XIV, we present our conclusions and discussions.

II. THE MOMENTUM KICK MODEL

It should be pointed out on the outset that the interaction between a jet and the medium can be described by representing the medium either as fields or as particles. In our momentum kick model, we choose to represent the medium as particles. We describe the interaction between the jet and the medium in terms of jet-(medium parton) collisions, from which each collided medium parton receives a momentum kick and subsequently materializes as a ridge particle. We have been guided to such a particle description because of the strong color screening in a dense color medium [52, 53]. The presence of the azimuthal kinematic correlation between the jet and the ridge particles lends additional support to the concept of jet-(medium parton) collisions as a central element of the phenomenon.

As depicted in Fig. 1, the main contents of the momentum kick model can be briefly summarized as follows:

1. A near-side jet parton emerges near the medium surface and the jet parton collides with medium partons on its way to the detector. It loses energy by collisions and gluon radiation. It subsequently fragments into the trigger particle and other associated fragmentation products.
2. Each jet-(medium parton) collision imparts a momentum kick \mathbf{q} to the initial medium parton of momentum \mathbf{p}_i in the general direction of the trigger particle to change it to the final parton momentum $\mathbf{p} \equiv \mathbf{p}_f = \mathbf{p}_i + \mathbf{q}$, and it modifies the normalized initial parton momentum distribution $dF/d\mathbf{p}_i$ to become the final parton momentum distribution $dF/d\mathbf{p}_f$. The kicked partons subsequently materialize by parton-hadron duality as ridge particles.

Based on the above picture, we can describe the jet and the kicked particles in quantitative terms. We consider a nucleus-nucleus collision at a given impact parameter b with N_{bin} binary nucleon-nucleon collisions, and we label a binary collision by the index i . For the i th binary collision, there is a jet parton distribution $dN_j^i/d\mathbf{p}_j$ where the subscript j stands for the ‘‘jet parton’’. The sum over all binary collisions for a given impact parameter leads to the total jet parton distribution $dN_j/d\mathbf{p}_j$ defined by

$$\frac{dN_j}{d\mathbf{p}_j} = \sum_{i=1}^{N_{\text{bin}}} \frac{dN_j^i}{d\mathbf{p}_j}. \quad (1)$$

In a single pp collision, the yield of a trigger particle with momentum \mathbf{p}_{trig} is

$$\frac{dN^{pp}}{d\mathbf{p}_{\text{trig}}}(\mathbf{p}_{\text{trig}}) = \int d\mathbf{p}_j \frac{dN^{pp}}{d\mathbf{p}_j} \tilde{D}(\mathbf{p}_{\text{trig}}, \mathbf{p}_j), \quad (2)$$

where $\tilde{D}(\mathbf{p}_{\text{trig}}, \mathbf{p}_j)$ is the fragmentation function for fragmenting a trigger hadron of momentum \mathbf{p}_{trig} out of a parent jet parton of momentum \mathbf{p}_j . For convenience of accounting in nucleus-nucleus collisions for a fixed \mathbf{p}_{trig} , we rescale the fragmentation function by dividing the above equation by the quantity on the lefthand side, $[dN^{pp}/d\mathbf{p}_{\text{trig}}(\mathbf{p}_{\text{trig}})]$, to change the above equation to

$$1 = \int d\mathbf{p}_j \frac{dN^{pp}}{d\mathbf{p}_j} D(\mathbf{p}_{\text{trig}}, \mathbf{p}_j), \quad (3)$$

where the re-normalized fragmentation function $D(\mathbf{p}_{\text{trig}}, \mathbf{p}_j)$ is

$$D(\mathbf{p}_{\text{trig}}, \mathbf{p}_j) = \tilde{D}(\mathbf{p}_{\text{trig}}, \mathbf{p}_j) / [dN^{pp}/d\mathbf{p}_{\text{trig}}(\mathbf{p}_{\text{trig}})]. \quad (4)$$

Using the fragmentation function normalized in this manner, a binary nucleon-nucleon collision (the i -th binary collision, say) produces a single trigger particle at the momentum \mathbf{p}_{trig} , in the absence of jet-medium interactions,

$$\int d\mathbf{p}_j \frac{dN_j^i}{d\mathbf{p}_j} D(\mathbf{p}_{\text{trig}}; \mathbf{p}_j) = (\text{unquenched } N_{\text{trig}} \text{ arising from the } i\text{th binary collision}) = 1. \quad (5)$$

With the total jet source distribution $dN_j/d\mathbf{p}_j$ coming from all binary collisions in a nucleus-nucleus collision, we have

$$N_{\text{bin}} = \int d\mathbf{p}_j \frac{dN_j}{d\mathbf{p}_j} D(\mathbf{p}_{\text{trig}}; \mathbf{p}_j). \quad (6)$$

In the presence of jet-medium interactions, the total number of trigger particles N_{trig} with momentum \mathbf{p}_{trig} is

$$N_{\text{trig}} = \int d\mathbf{p}_j \frac{dN_j}{d\mathbf{p}_j} \sum_{N=0}^{N_{\text{max}}} P(N) e^{-\zeta_a N} D(\mathbf{p}_{\text{trig}}; \mathbf{p}_j - \sum_{n=1}^N \mathbf{q}_n - \mathbf{\Delta}_r), \quad (7)$$

where N is the number of medium partons kicked by a jet of momentum \mathbf{p}_j along its way, N_{max} is the maximum N considered, and $P(N)$ is a probability distribution of N , normalized by $\sum_{N=0}^{N_{\text{max}}} P(N) = 1$. The factor $e^{-\zeta_a N}$ describes the absorption of the jet due to the inelastic fraction of jet-(medium parton) collisions. The quantity \mathbf{q}_n is the momentum kick on the medium parton due to the n th jet-(medium parton) collision, and $\mathbf{\Delta}_r$ is the jet momentum loss due to the gluon radiation of the jet. We shall postpone our discussion of $P(N)$ to Section XII. It suffices to indicate here that $P(N)$ depends on the medium parton density along the trajectory and the jet-(medium parton) scattering cross section.

As is obvious from Eq. (7), the number of trigger particles N_{trig} in a nucleus-nucleus collision (with the momentum \mathbf{p}_{trig}) will be equal to the number of binary collisions N_{bin} in the absence of any jet-medium interaction,

$$N_{\text{trig}}(\{\zeta_a, \mathbf{q}_n, \mathbf{\Delta}_r\} = 0) = N_{\text{bin}}. \quad (8)$$

The ratio of $N_{\text{trig}}(\{\zeta_a, \mathbf{q}_n, \mathbf{\Delta}_r\} \neq 0)$ in a nucleus-nucleus collision with respect to $N_{\text{trig}}(\{\zeta_a, \mathbf{q}_n, \mathbf{\Delta}_r\} = 0)$ in the absence of any jet-medium interaction is the R_{AA} measure of jet quenching,

$$R_{AA} = \frac{1}{N_{\text{bin}}} \int d\mathbf{p}_j \frac{dN_j}{d\mathbf{p}_j} \sum_{N=0}^{N_{\text{max}}} P(N) e^{-\zeta_a N} D(\mathbf{p}_{\text{trig}}; \mathbf{p}_j - \sum_{n=1}^N \mathbf{q}_n - \mathbf{\Delta}_r). \quad (9)$$

Because the kicked partons are identified as ridge particles by parton-hadron duality and two-third of the produced hadrons are charged, the distribution of associated ridge particles is therefore

$$\frac{dN_{\text{ridge}}^{AA}}{d\mathbf{p}} = \int d\mathbf{p}_j \frac{dN_j}{d\mathbf{p}_j} \sum_{N=1}^{N_{\text{max}}} P(N) e^{-\zeta_a N} D(\mathbf{p}_{\text{trig}}; \mathbf{p}_j - \sum_{n=1}^N \mathbf{q}_n - \mathbf{\Delta}_r) \left\{ \frac{2}{3} \sum_{n=1}^N f_{Rn} \frac{dF_n}{d\mathbf{p}}(\mathbf{q}_n) \right\}, \quad (10)$$

where $0 < f_{Rn} \leq 1$ is the ridge attenuation factor for the n -th kicked parton to reach the detector and $dF_n/d\mathbf{p}$ is the normalized momentum distribution of the n -th kicked medium parton, normalized to $\int d\mathbf{p} dF_n/d\mathbf{p} = 1$. We note that the righthand sides of Eq. (7) and (10) differ only by the quantity in the curly bracket. It is convenient to define the expectation value $\langle \mathcal{O} \rangle$ of a quantity \mathcal{O} in the presence of the jet distribution, jet momentum loss, and jet fragmentation by

$$\begin{aligned} \langle \mathcal{O} \rangle &= \int d\mathbf{p}_j \frac{dN_j}{d\mathbf{p}_j} \sum_{N=1}^{N_{\text{max}}} P(N) e^{-\zeta_a N} D(\mathbf{p}_{\text{trig}}; \mathbf{p}_j - \sum_{n=1}^N \mathbf{q}_n - \mathbf{\Delta}_r) \mathcal{O} \\ &\div \int d\mathbf{p}_j \frac{dN_j}{d\mathbf{p}_j} \sum_{N=1}^{N_{\text{max}}} P(N) e^{-\zeta_a N} D(\mathbf{p}_{\text{trig}}; \mathbf{p}_j - \sum_{n=1}^N \mathbf{q}_n - \mathbf{\Delta}_r). \end{aligned} \quad (11)$$

Using this definition, the momentum distribution of the ridge particle momentum distribution per trigger particle is then the expectation value of the sum of the final momentum distribution of the kicked medium partons:

$$\frac{1}{N_{\text{trig}}} \frac{dN_{\text{ridge}}^{AA}}{d\mathbf{p}} = \left\langle \frac{2}{3} \sum_{n=1}^N f_{Rn} \frac{dF_n}{d\mathbf{p}}(\mathbf{q}_n) \right\rangle. \quad (12)$$

The above equation can be re-written as

$$\frac{1}{N_{\text{trig}}} \frac{dN_{\text{ridge}}^{AA}}{d\mathbf{p}} = \frac{2}{3} \left\{ \langle f_R \rangle \langle N \rangle \left\langle \frac{dF}{d\mathbf{p}} \right\rangle + \left\langle \sum_{n=1}^N (f_{Rn} - \langle f_R \rangle) \left[\frac{dF_n}{d\mathbf{p}}(\mathbf{q}_n) - \left\langle \frac{dF}{d\mathbf{p}} \right\rangle \right] \right\rangle \right\}, \quad (13)$$

where f_R is the average attenuation factor, $f_R = \sum_{n=1}^N f_{nR}/N$, and $\langle N \rangle$ is the expectation value of the total number of kicked medium partons per trigger particle. The quantity $\langle N \rangle$ is also the expectation value of the number of jet-(medium parton) collisions per trigger particle. We shall often label $\langle N \rangle$ alternatively as $\langle N_k \rangle$ with the subscript k to emphasize that this is the averaged number of kicked medium partons per trigger.

As defined by Eq. (11), $\langle N \rangle$ and $\langle N_k \rangle$ are given by

$$\langle N \rangle \equiv \langle N_k \rangle = \frac{1}{N_{\text{trig}}} \int d\mathbf{p}_j \frac{dN_j}{d\mathbf{p}_j} \sum_{N=0}^{N_{\text{max}}} NP(N) e^{-\zeta_\alpha N} D(\mathbf{p}_{\text{trig}}; \mathbf{p}_j - \sum_{n=1}^N \mathbf{q}_n - \mathbf{\Delta}_r). \quad (14)$$

To understand the gross features of the phenomenon, we neglect the second term in the curly bracket of Eq. (13) which arises from the fluctuation of the quantities from their mean values. The formulation can also be simplified by taking the different momentum kicks \mathbf{q}_n to be the average \mathbf{q} . Using these simplifying assumptions, we then obtain

$$\frac{1}{N_{\text{trig}}} \frac{dN_{\text{ridge}}^{AA}}{d\mathbf{p}} = \langle f_R \rangle \frac{2}{3} \langle N_k \rangle \left\langle \frac{dF}{d\mathbf{p}} \right\rangle. \quad (15)$$

Thus, the ridge particle distribution is separated into a geometry-dependent part $\langle f_R \rangle (2/3) \langle N_k \rangle$ and the average normalized momentum distribution of ridge particles, $\langle dF/d\mathbf{p} \rangle$. For brevity of notation, the bracket symbol, $\langle \rangle$, for $\langle dF/d\mathbf{p} \rangle$ will be made implicit, and the normalized ridge momentum distribution $dF/d\mathbf{p}$ will be understood to represent the average over the jet source distribution, jet collision locations, and jet energies.

If one is interested in the total ridge yield by integrating over the ridge particle momentum, we then get

$$\frac{N_{\text{ridge}}^{AA}}{N_{\text{trig}}} = \langle f_R \rangle \frac{2}{3} \langle N_k \rangle. \quad (16)$$

Our strategy is to study first the case of the most-central AuAu collisions at $\sqrt{s_{NN}} = 200$ GeV where the momentum distribution of the ridge particles and the average number of kicked medium partons can be inferred from experimental data [5, 7, 9]. In Sections XI, XII, and XIII, we shall then examine the average number of kicked medium partons and the experimental ridge yield as a function of centrality, collision energies, and nuclear mass numbers [7, 8, 14], using the number of kicked medium partons for the most-central AuAu collision at $\sqrt{s_{NN}} = 200$ GeV as a reference.

III. RELATION BETWEEN THE INITIAL AND FINAL MOMENTUM DISTRIBUTIONS

In the momentum kick model, the normalized final parton momentum distribution $E dF/d\mathbf{p}$ at \mathbf{p} is related to the normalized initial parton momentum distribution $E_i dF/d\mathbf{p}_i$ at \mathbf{p}_i at a shifted momentum, $\mathbf{p}_i = \mathbf{p} - \mathbf{q}$, and we have [19]

$$\frac{dF}{p_t dp_t d\eta d\phi} = \left[\frac{dF}{p_{ti} dp_{ti} dy_i d\phi_i} \frac{E}{E_i} \right]_{\mathbf{p}_i = \mathbf{p} - \mathbf{q}} \sqrt{1 - \frac{m^2}{(m^2 + p_t^2) \cosh^2 y}}, \quad (17)$$

where the factor E/E_i insures conservation of particle numbers and the last factor changes the rapidity distribution to the pseudorapidity distribution [45]. The momentum kick \mathbf{q} is expected to lie within a narrow cone in the trigger particle direction for a high-energy jet. To minimize the number of parameters, we approximate \mathbf{q} to lie along the trigger particle direction.

To relate the final parton momentum distribution to the observed hadron momentum distribution, we assume hadron-parton duality which is a reasonable description for the hadronization of energetic partons. The final parton momentum distribution Eq. (17), multiplied by $\langle f_R \rangle (2/3) \langle N_k \rangle$, can then be identified with the observed (charged) hadron associated particle momentum distribution per trigger, $dN_{\text{ch}}/N_{\text{trig}} d\eta d\phi p_t dp_t$, as given by Eq. (15). By a simple change of variables, we can further obtain $dN_{\text{ch}}/N_{\text{trig}} d\Delta\eta d\Delta\phi p_t dp_t$ in terms of $\Delta\eta = \eta - \eta_{\text{jet}}$ and $\Delta\phi = \phi - \phi_{\text{jet}}$, relative to the trigger particle. The basic ingredients of the momentum kick model are then the magnitude of the momentum kick q , the normalized initial parton momentum distribution $dF/d\mathbf{p}_i$, and the average number of jet-(medium parton) collisions per jet. For numerical calculations, we set $m = m_\pi$.

The initial and final parton momenta can be represented in terms of Cartesian components in the collider frame, $\mathbf{p} = (p_1, p_2, p_3)$, with a longitudinal p_3 component, a transverse p_1 component, and another transverse p_2 component perpendicular to both p_1 and p_3 . The coordinate axes can be so chosen that the trigger jet lies in the p_1 - p_3 plane. The initial parton momentum $\mathbf{p}_i = (p_{i1}, p_{i2}, p_{i3})$ is related to the final momentum $\mathbf{p}_f = (p_{f1}, p_{f2}, p_{f3})$ and the trigger jet rapidity η_{jet} by

$$p_{i1} = p_{f1} - \frac{q}{\cosh \eta_{\text{jet}}}, \quad (18a)$$

$$p_{i2} = p_{f2}, \quad (18b)$$

$$p_{i3} = p_{f3} - \frac{q \sinh \eta_{\text{jet}}}{\cosh \eta_{\text{jet}}}. \quad (18c)$$

For a given trigger particle pseudorapidity, these relations allow one to obtain \mathbf{p}_i from $\mathbf{p}_f = \mathbf{p}$ for the evaluation of the ridge yield per trigger particle.

IV. PARAMETRIZATION OF THE INITIAL PARTON MOMENTUM DISTRIBUTION

As the jet-(medium parton) collisions take place at different spatial and temporal locations during the passage of the near-side jet through the medium, the initial momentum distribution $E_i dF/d\mathbf{p}_i$ in Eq. (17) refers actually to an average over spatial and temporal regions during the early stage of the nucleus-nucleus collision. The ‘initial’ momentum distribution can also be called the ‘early’ parton momentum distribution. This initial parton momentum distribution $E_i dF/d\mathbf{p}_i$ of the medium partons at the time of jet-(medium parton) collisions is not yet a quantity that can be obtained from first principles of QCD, although some of its qualitative features can be inferred from basic principles as will be discussed in Sections VIII and IX. Furthermore, jets occur at an early stage of the nucleus-nucleus collisions, whereas the momentum distribution of the bulk medium pertains to the state of the medium at the end-point of the nucleus-nucleus collision. Therefore the early parton momentum distribution near the beginning stage of the nucleus-nucleus collision needs not be the same as that of the bulk matter at the end-point of the nucleus-nucleus collision.

Under the circumstances, the parton momentum distribution at the early stage of the nucleus-nucleus collision can only be obtained phenomenologically from the ridge particle data by representing it as a simple function whose distinct characteristics can be determined by comparison with experimental ridge data.

The initial momentum distribution was parametrized previously as $e^{-y_i^2/2\sigma_y^2} \exp\{-\sqrt{m^2 + p_{ti}^2}/T\}/\sqrt{m^2 + p_{ti}^2}$, with m taken to be m_π [19]. Although this is adequate for mid-rapidity and high- p_t ridge particles [19], it leads to too large a ridge yield both at $p_t \sim 1$ GeV (dotted curve in Fig. 2) and at forward rapidities. Our understanding of the behavior of the early parton transverse momentum distribution has not reached such a stage that we can predict its low p_t behavior definitively. If the partons arise from a deconfined medium with a finite transverse boundary, then the transverse parton momentum distribution at small p_t will be flattened from an exponential distribution, as shown in Figs. 1 and 2 of [54]. Transverse distributions of this type can be described by replacing the denominator $\sqrt{m^2 + p_{ti}^2}$ with $\sqrt{m_d^2 + p_{ti}^2}$ where m_d can be adjusted to lead to the correct ridge yield at $p_t \sim 1$ GeV. The extracted transverse momentum distribution may provide useful information to study the transverse radius of the deconfined parton medium [54, 55].

The difficulty with the forward rapidity region can be resolved by noting that the Gaussian rapidity distribution of [19] does not take into account the kinematic boundary restrictions on phase space. The large values of σ_y extracted from the mid-rapidity data in [19] imply that the rapidity distribution is quite flat in the mid-rapidity region. We can use a rapidity distribution that retains the flatness at mid-rapidity but also respects the kinematic boundaries at large rapidities and large p_t . Accordingly, we parametrize the normalized initial parton momentum distribution as

$$\frac{dF}{p_{ti} dp_{ti} dy_i d\phi_i} = A_{\text{ridge}} (1-x)^a \frac{e^{-\sqrt{m^2 + p_{ti}^2}/T}}{\sqrt{m_d^2 + p_{ti}^2}}, \quad (19)$$

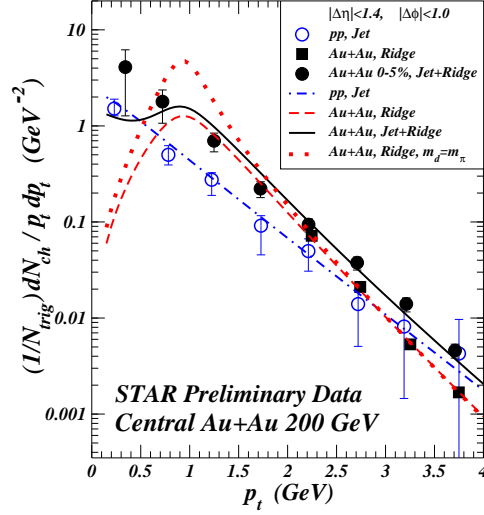


FIG. 2: (Color online) The symbols represent STAR experimental data [5, 7] and the curves theoretical results of $dN_{ch}/N_{trig}p_t dp_t$, for pp and central AuAu collisions.

where A_{ridge} is a normalization constant defined (and determined numerically) by

$$\int dy_i d\phi_i p_{ti} dp_{ti} A_{ridge} (1-x)^a \frac{\exp\{-\sqrt{m^2 + p_{ti}^2}/T\}}{\sqrt{m_d^2 + p_{ti}^2}} = 1. \quad (20)$$

In Eq. (19), x is the light-cone variable [45]

$$x = \frac{\sqrt{m^2 + p_{ti}^2}}{m_b} e^{|y_i - y_b|}, \quad (21)$$

a is the fall-off parameter that specifies the rate of decrease of the distribution as x approaches unity, y_b is the beam parton rapidity, and m_b is the mass of the beam parton whose collision and separation lead to the inside-outside cascade picture of particle production [42, 43, 44, 45, 46]. As $x \leq 1$, there is a kinematic boundary that is a function of y_i and p_{ti} ,

$$\sqrt{m^2 + p_{ti}^2} = m_b e^{y_b - |y_i|}. \quad (22)$$

We expect y_b to have a distribution centered around the nucleon rapidity, $y_N = \cosh^{-1}(\sqrt{s_{NN}}/2m_N)$. For lack of a definitive determination, we shall set y_b equal to y_N and m_b equal to m_π , pending their future experimental determination by examining the ridge boundaries. This form of the initial parton distribution leads to a restricted phase space that is smaller than that for a Gaussian rapidity distribution. As a consequence, it can lead to a smaller associated particle yield that agrees with experimental forward rapidity data as shown in Section VI.

V. PARTICLE MOMENTUM DISTRIBUTION OF THE JET COMPONENT

As a jet passes through the parton medium, the medium partons kicked by the jet will materialize to become particles in the associated ‘‘ridge component’’, while the jet will fragment and radiate into the trigger and associated ‘‘jet component’’ particles. If the contribution from the jet component is known, we can separate out the ridge component using experimental data of total associated particles. The distribution of the ‘‘jet component’’ of (charged) associated fragmentation products is given by

$$\frac{dN_{jet}^{AA}}{d\mathbf{p}} = \int d\mathbf{p}_j \frac{dN_j}{d\mathbf{p}_j} \sum_{N=0}^{N_{max}} P(N) e^{-\zeta_a N} D_2(\mathbf{p}_{trig}, \mathbf{p}; \mathbf{p}_j - \sum_{n=1}^N \mathbf{q}_n - \Delta_r), \quad (23)$$

where $D_2(\mathbf{p}_a, \mathbf{p}_b; \mathbf{p}_c)$ is the double fragmentation function for fragmenting into hadrons of momentum \mathbf{p}_a and \mathbf{p}_b from a jet parton of momentum \mathbf{p}_c . Fragmentation measurements [7] suggest an approximate scaling relation

$$D_2(\mathbf{p}_{trig}, \mathbf{p}; \mathbf{p}_c) \approx D(\mathbf{p}_{trig}; \mathbf{p}_c) D_z(\mathbf{p}; \mathbf{p}_{trig}), \quad (24)$$

where $D_z(\mathbf{p}; \mathbf{p}_{\text{trig}})$ is approximately the same (within a factor of about 0.6 to 1.2) for dAu and AuAu collisions in $2.5 < p_{t,\text{trig}} < 6$ GeV (Fig. 5b and 5c of [7]). By applying this approximate scaling relation to Eq. (23) and using Eq. (7), the (charged) jet component in an AA central collision per trigger is

$$\frac{1}{N_{\text{trig}}} \frac{dN_{\text{jet}}^{AA}}{d\mathbf{p}} \approx D_z(\mathbf{p}; \mathbf{p}_{\text{trig}}) \approx \frac{dN_{\text{jet}}^{pp}}{d\mathbf{p}}. \quad (25)$$

Because of the approximate nature of the above relation (up to a factor of about 0.6 to 1.2), we need to make a quantitative check. In the region where the jet component has a prominent appearance, as in Fig. 3(d) for $2 < p_t < 4$ GeV, the total $dN_{\text{ch}}/N_{\text{trig}}d\Delta\eta$ distribution at $\Delta\eta \sim 0$ has indeed a shape similar to, but a peak magnitude about equal to, the pp near-side jet distribution. The total yield is the sum of the jet component and the ridge yield, and the ridge yield at $\Delta\eta \sim 0$ is non-zero and nearly flat (Fig. 3(d)). The near-side jet component in AuAu central collisions per trigger is thus an attenuated pp near-side jet distribution, as expected for production in an interacting medium. If one assumes that fragmentation products lying deeper than an absorption length from the surface are all absorbed, then the average jet fragment attenuation factor is $f_J = \int_0^\lambda e^{-x/\lambda} dx/\lambda = 0.632$, which leads semi-empirically to a reasonable description of the experimental data as indicated below in Figs. 2 and 3.

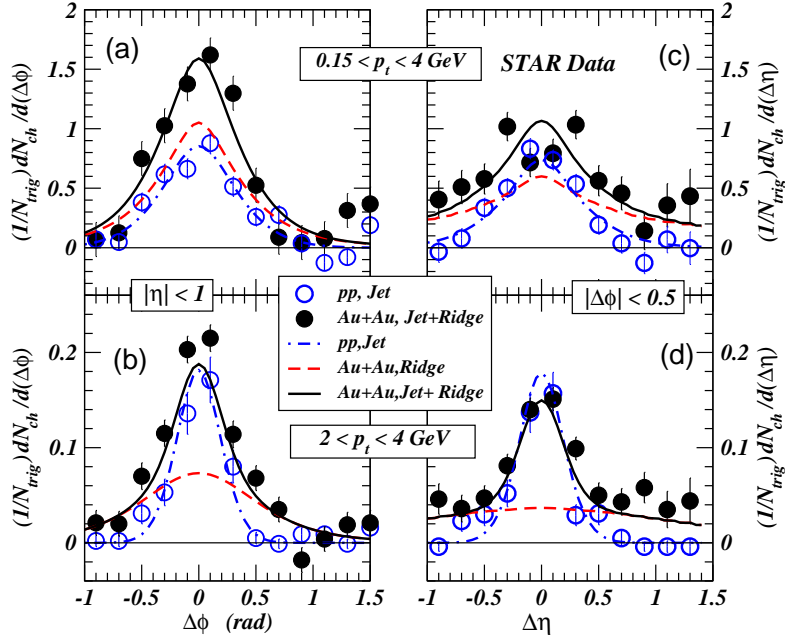


FIG. 3: (Color online) The symbols represent experimental data [5] and the curves theoretical results, for pp and central AuAu collisions. (a) and (b) give the $dN_{\text{ch}}/N_{\text{trig}}d\Delta\phi$ distributions. (c) and (d) give the $dN_{\text{ch}}/N_{\text{trig}}d\Delta\eta$ distributions.

The sum of the distributions (15) and (25), relative to the trigger particle η_{jet} and ϕ_{jet} , is therefore given more precisely as

$$\left[\frac{1}{N_{\text{trig}}} \frac{dN_{\text{ch}}}{p_t dp_t d\Delta\eta d\Delta\phi} \right]_{\text{total}}^{AA} = \left[\langle f_R \rangle \frac{2}{3} \langle N_k \rangle \frac{dF}{p_t dp_t d\Delta\eta d\Delta\phi} \right]_{\text{ridge}}^{AA} + \left[f_J \frac{dN_{\text{jet}}^{pp}}{p_t dp_t d\Delta\eta d\Delta\phi} \right]_{\text{jet}}^{AA}. \quad (26)$$

The experimental momentum distribution of (charged) near-side particles associated with the trigger in a pp collision, measured relative to the trigger jet, can be parametrized as

$$\frac{dN_{\text{jet}}^{pp}}{p_t dp_t d\Delta\eta d\Delta\phi} = N_{\text{jet}} \frac{\exp\{(m - \sqrt{m^2 + p_t^2})/T_{\text{jet}}\}}{T_{\text{jet}}(m + T_{\text{jet}})} \frac{1}{2\pi\sigma_\phi^2} e^{-[(\Delta\phi)^2 + (\Delta\eta)^2]/2\sigma_\phi^2}, \quad (27)$$

where N_{jet} is the number of (charged) near-side jet particles in a pp collision, and T_{jet} is the jet inverse slope (“temperature”) parameter. The above functional form of the jet fragmentation product cone in terms of $\Delta\phi$ and $\Delta\eta$ was chosen because $p_2 = p_t \sin \Delta\phi$ and $p_3 = p_t \sinh \Delta\eta$, and the square of the momentum perpendicular to the jet direction has a magnitude

$$p_2^2 + p_3^2 = p_t^2 \sin^2 \Delta\phi + p_t^2 \sinh^2 \Delta\eta \sim p_t^2 [(\Delta\phi)^2 + (\Delta\eta)^2] \quad \text{for small } \Delta\phi \text{ and } \Delta\eta. \quad (28)$$

The above equation indicates the symmetry between $\Delta\phi$ and $\Delta\eta$ for a narrow jet cone. In this functional form of Eq. (27) for the jet cone, the width in $\Delta\eta$ is equal to the width in $\Delta\phi$.

In our search for parameter values we find that the width parameter σ_ϕ depends slightly on p_t which we parametrize as

$$\sigma_\phi = \sigma_{\phi 0} \frac{m_a}{\sqrt{m_a^2 + p_t^2}}. \quad (29)$$

Experimental data for near-side jet particles in pp and central AuAu collisions obtained by the STAR Collaboration, within the detector acceptance of $|\eta_{\text{associated}}| < 1$ and $|\eta_{\text{jet}}| < 0.7$, are given in Figs. 2 and 3 [5]. Figure 2 gives the $dN_{\text{ch}}/N_{\text{trig}}p_t dp_t$ data, obtained by integrating $dN_{\text{ch}}/N_{\text{trig}}p_t dp_t d\Delta\phi d\Delta\eta$ over the domain of $|\Delta\eta| < 1.4$ and $|\Delta\phi| < 1.0$. Figures 3(a) and 3(b) give $dN_{\text{ch}}/N_{\text{trig}}d\Delta\phi$ data, and Figures 3(c) and 3(d) give $dN_{\text{ch}}/N_{\text{trig}}d\Delta\eta$ data. They are obtained by integrating $dN_{\text{ch}}/N_{\text{trig}}p_t dp_t d\Delta\phi d\Delta\eta$ over the domains indicated in the figures. Specifically, Fig. 3(a) covers the domain of $|\eta| < 1$ and $0.15 < p_t < 4$ GeV, 3(b) the domain of $|\eta| < 1$ and $2 < p_t < 4$, 3(c) the domain of $|\Delta\phi| < 0.5$ and $0.15 < p_t < 4$ GeV, and finally 3(d) the domain of $|\Delta\phi| < 0.5$ and $2 < p_t < 4$ GeV. The domains of integration in a pp collision and a nucleus-nucleus collision are the same, and the distribution in $\Delta\eta$ has been corrected for detector acceptance.

The set of experimental pp near-side jet data of $dN_{\text{ch}}^{pp}/p_t dp_t$, $dN_{\text{ch}}^{pp}/d\Delta\phi$, and $dN_{\text{ch}}^{pp}/d\Delta\eta$, represented by open circle points in Figs. 2 and 3, can be described by Eqs. (27) and (29), with the following parameters

$$T_{\text{jet}} = 0.55 \text{ GeV}, \quad \sigma_{\phi 0} = 0.50, \quad m_a = 1.1 \text{ GeV}, \quad \text{and} \quad N_{\text{jet}} = 0.75. \quad (30)$$

Theoretical pp jet results obtained with this set of parameters within the specified experimental domain are shown as the dash-dot curves in Figs. 2 and 3. They yield a reasonable description of the experimental momentum distributions of jet particles associated with the near-side jet in a pp collision.

VI. COMPARISON OF THEORETICAL NEAR-SIDE ASSOCIATED PARTICLE YIELDS WITH EXPERIMENT

Theoretical evaluation of both the jet component and the ridge component for central AuAu collisions allows one to determine the total yield of associated particles as determined by Eq. (26). A self-consistent search for the initial parton momentum distribution in Eqs. (19) and (17) can be made by comparing the momentum kick model results with experimental data for $dN_{\text{ch}}/N_{\text{trig}}p_t dp_t$, $dN_{\text{ch}}/N_{\text{trig}}d\Delta\phi$, and $dN_{\text{ch}}/N_{\text{trig}}d\Delta\eta$ for mid-rapidities in Figs. 2 and 3, and $dN_{\text{ch}}/N_{\text{trig}}d\Delta\phi$ for forward rapidities in Fig. 4. We find that the totality of the STAR associated particle data, from $p_t = 0.15$ GeV to 4 GeV and η from zero up to 3.9 in central AuAu collisions at $\sqrt{s_{NN}} = 200$ GeV [6, 7, 9], can be described by Eqs. (26) and (17) with parameters

$$q = 1.0 \text{ GeV}, \quad \text{and} \quad \langle f_R \rangle \langle N_k \rangle = 3.8, \quad (31)$$

in conjunction with the initial parton momentum distribution Eq. (19) with parameters

$$T = 0.50 \text{ GeV}, \quad m_d = 1 \text{ GeV}, \quad \text{and} \quad a = 0.5. \quad (32)$$

We now discuss the comparison of the experimental data with theoretical results involved in the above analysis. In Fig. 2 the STAR experimental $dN_{\text{ch}}/N_{\text{trig}}p_t dp_t$ data [5, 7] are represented by solid circular points for central AuAu collisions and by open circle points for pp collisions. The theoretical results for pp collisions obtained with the parametrization of Eq. (27) with parameters in Eq. (30) are shown as the dash-dot curves, which agree with pp near-side data in all experimental kinematic regions. Experimental ridge $dN_{\text{ch}}/N_{\text{trig}}p_t dp_t$ data in central AuAu collisions [7] are also shown as solid squares and they are calibrated by using the data of Fig. 2 of [7]. The solid curve is the theoretical result for $dN_{\text{ch}}/N_{\text{trig}}p_t dp_t$ for central AuAu collisions, as the sum of the jet part and the ridge part, with the ridge part of the contribution shown as the dashed curve. They have been calculated with $m_d = 1$ GeV. If we set m_d equal to m_π , then we will get the ridge yield represented by the dotted curve, which over-predicts the ridge yield at $p_t \sim 1$ GeV.

Fig. 2 shows good agreement between theoretical $dN_{\text{ch}}/N_{\text{trig}}p_t dp_t$ with experimental data for central AuAu collisions. The theoretical transverse momentum distribution of the jet and the ridge components have very different shapes in the low p_t region. The jet component $dN_{\text{ch}}/N_{\text{trig}}p_t dp_t$ decreases exponentially as a function of increasing p_t . On the other hand, the magnitude of the final transverse parton momentum p_{tf} is greater than the initial transverse momentum p_{ti} approximately by the amount q . The initial momentum distribution $dF/p_{ti} dp_{ti}$ has a peak at $p_{ti} = 0$. As a consequence, the theoretical ridge yield of final partons, $dN_f/N_{\text{trig}}p_{tf} dp_{tf}$, has a peak around $p_{tf} \sim q \sim 1$ GeV and it decreases significantly for small values of p_t , in contrast to the exponential behavior of the jet component.

It is interesting to note that the theoretical ratio of the jet yield to the ridge yield is greater than 1 for $p_t \lesssim 0.6$ GeV, but is less than 1 in the interval $0.6 \lesssim p_t \lesssim 3.7$ GeV. The ratio reverts to become greater than 1 at 3.7 GeV $\lesssim p_t$. The change of the dominance of the ridge component as p_t changes may lead to experimentally observable variations of the shape of the $dN_{\text{ch}}/N_{\text{trig}}d\Delta\eta$ as a function of p_t .

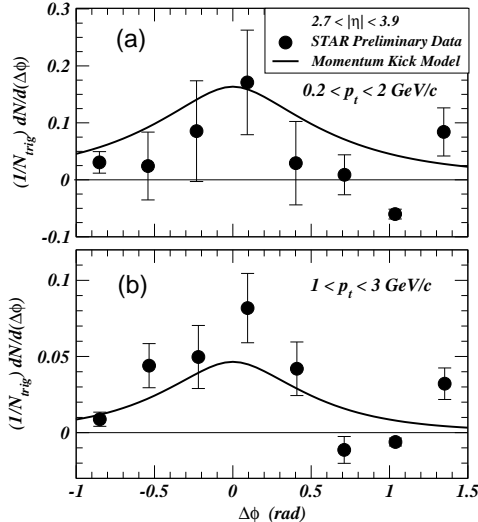


FIG. 4: (Color online) Azimuthal angular distribution data at forward pseudorapidities for central AuAu collisions from the STAR Collaboration [9], compared with theoretical results shown as solid curves from the momentum kick model. (a) is for $0.20 < p_t < 2$ GeV, and (b) is for $1 < p_t < 3$ GeV.

In Fig. 3, the experimental total associated particle yields [5, 9] are represented by solid circular points for central AuAu collisions and by open circles for pp collisions. The theoretical results for pp collisions obtained with the parametrization of Eq. (27) are shown as the dash-dot curves which agree with experimental pp near-side data. In these figures, the theoretical total yield and the ridge yield for central AuAu collisions are represented by solid and dashed curves, respectively. Comparison of the theoretical total yield and the experimental total associated particle yield for central AuAu collisions indicates general agreement over all azimuthal angles [Figs. 3(a) and 3(b)] and over all pseudorapidities [Figs. 3(c) and 3(d)], for both $0.15 < p_t < 4$ GeV [Figs. 3(a) and 3(c)] and $2 < p_t < 4$ GeV [Figs. 3(b) and 3(d)].

One notes from Fig. 3(a) that for the region of $0.15 < p_t < 4$ GeV, which receives the dominant contributions from the low p_t region, the widths of the azimuthal angular distributions of the ridge and the jet components are nearly the same, with the magnitude of the ridge yield slightly higher than the pp yield. On the other hand, in the region of $2 < p_t < 4$ GeV in Fig. 3(b), which receives the dominant contributions from the region near $p_t \sim 2$ GeV, the azimuthal angular distributions of the jet component is narrower than the ridge component azimuthal angular distribution.

We observe from Fig. 3(c) that the theoretical AuAu jet and ridge components have different shapes in $dN_{\text{ch}}/N_{\text{trig}}d\Delta\eta$. The jet component maintains a sharp peak in $dN_{\text{ch}}/N_{\text{trig}}d\Delta\eta$. In the low p_t region, the pseudorapidity distribution of the theoretical ridge component is significantly broader than the jet component and its magnitude remains to have a non-zero value at large $|\Delta\eta|$. In the high p_t region in Fig. 3(d), the ridge pseudorapidity distribution is essentially flat and non-zero. The broad peak structure for the low p_t region comes from the factor E/E_i in Eq. (17), arising from the difference of the momenta of the parton before and after the collision. This factor is close to 1 for the high p_t region, and the flatness of the distribution is a reflection of the initial rapidity distribution.

We turn now to forward rapidities where preliminary experimental data for central AuAu collisions have been obtained for $2.7 < |\eta| < 3.9$ [9]. We note that $dN_{\text{ch}}/N_{\text{trig}}d\Delta\phi d\Delta\eta$ at $\Delta\phi \sim 0$ for $|\eta| < 1$ in Fig. 3(a) is an order of magnitude greater than the corresponding $dN_{\text{ch}}/N_{\text{trig}}d\Delta\phi d\Delta\eta$ for $2.7 < |\eta| < 3.9$ in Fig. 4(a). This implies a substantial fall-off of the ridge yield $dN_{\text{ch}}/N_{\text{trig}}d\Delta\phi d\Delta\eta$ at $\Delta\phi \sim 0$ in going from mid-rapidities to large rapidities. Even though the mid-rapidity data place a constraint on the flatness of the mid-rapidity distribution, they do not otherwise constrain the rate of fall-off of the distribution in the forward rapidity region. Measurements at forward rapidities in Fig. 4 contain events with large η and p_t that are either already outside the kinematic limits or close to the kinematic limits. Therefore, even with large errors, the forward rapidity data in Fig. 4 are sensitive to the constraint of the kinematic limits and the rate of fall-off of the initial parton momentum distribution as specified by the fall-off parameter a . The data of Fig. 4 lead to $a = 0.5$.

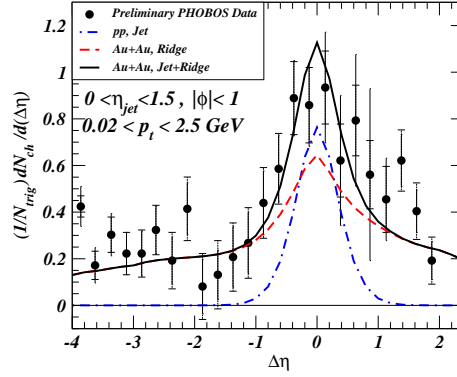


FIG. 5: (Color online) The momentum distribution of the associated particles as a function of the pseudorapidity relative to the jet pseudorapidity $\Delta\eta$. The solid circular points are the data from the PHOBOS Collaboration [18] and the curves give theoretical predictions from the momentum kick model. The solid, dashed, and dash-dot curves give the total yield, the ridge yield, and the pp jet yield, respectively.

Using the parameters we have extracted from the STAR ridge data as given by (31) and (32), we can predict the pseudorapidity distribution for the PHOBOS experimental acceptance defined by $\Delta\phi \leq 1$, $0 < \eta_{\text{trig}} < 1.5$, and $0.02 < p_t < 2.5$ GeV. The theoretical total associated particle yield, which is the sum of the ridge yield and the attenuated pp jet yield, is shown as the solid curve in Fig. 5. The theoretical pp jet yield and the ridge component of the associated particles are shown as the dash-dot and the dashed curves respectively. The result has been corrected for $\Delta\eta$ acceptance. The present prediction of the momentum kick model for the near-side jet associated particle yields was found to agree well with experimental measurements obtained by the PHOBOS Collaboration [18] up to large $|\Delta\eta|$ for the region of small p_t .

VII. EXTRACTED INITIAL PARTON MOMENTUM DISTRIBUTION

It is illuminating to examine the initial parton momentum distribution extracted from the totality of experimental data in Figs. 2, 3, and 4. We find that the normalized initial parton momentum distribution at the jet-(medium parton) collisions can be represented by $dF/dy d\phi p_t dp_t = A_{\text{ridge}}(1-x)^a \exp\{-\sqrt{m^2 + p_t^2}/T\}/\sqrt{m_d^2 + p_t^2}$, where $x = \sqrt{m^2 + p_t^2} e^{|y|-y_b}/m_b$, $a=0.5$, $T = 0.5$ GeV, and $m_d = 1$ GeV. Here, (y, ϕ, p_t) represent the initial parton momentum coordinates. We show explicitly the extracted, normalized initial parton distribution $dF/p_t dp_t dy$ at the moment of jet-(medium parton) collisions in Fig. 6. It is given as a function of p_t for various y in Fig. 6(a), and conversely as a function of y for various p_t in Fig. 6(b). It has a thermal-like transverse momentum distribution and is nearly flat in rapidity at $y \sim 0$, with sharp kinematic boundaries at large $|y|$.

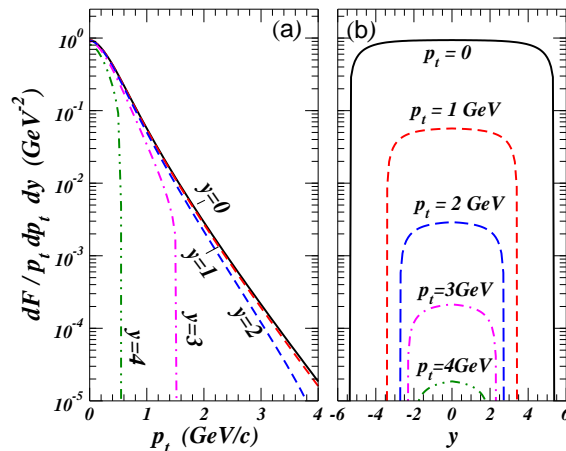


FIG. 6: (Color online) Normalized initial parton momentum distribution $dF/dyp_t dp_t$ extracted from the STAR Collaboration data [5, 7, 9]. (a) $dF/dyp_t dp_t$ as a function of p_t for different y , and (b) $dF/dyp_t dp_t$ as a function of y for different p_t .

In Fig. 6(a), the momentum distribution for $y = 0$ and high p_t has a slope parameter T that is intermediate between that of the jet and inclusive bulk particles. This indicates that partons at the moment of jet-(medium parton) collision is at an intermediate stage of dynamical equilibration.

The parton momentum distribution cannot be separated as the product of two independent distributions. The momentum distribution as a function of p_t depends on the rapidity variable y which affects the boundaries of the distribution. The distribution as a function of p_t does not change much for y up to $y = 2$. For $y = 3$, the maximum value of p_t is 1.54 GeV and the distribution changes significantly as the kinematic boundary is approached. For $y = 4$, the boundary of p_t is located at 0.55 GeV.

In Fig. 6(b), the momentum distribution as a function of y for a fixed p_t is essentially flat near central rapidities and it extends to a maximum value of $|y|_{\text{max}}$ that depends on p_t , as given by Eq. (22). The flat distribution changes rather rapidly as it approaches the kinematic limits. The kinematic boundary becomes more restrictive to cover a smaller allowed region of y as p_t increases. For example, for $p_t = 0, 1, 2, 3$, and 4 GeV, the maximum values of $|y|$ are 5.36, 3.4, 2.7, 2.33, and 2.05, respectively. The extracted early rapidity distribution exhibits the feature of a plateau structure in rapidity. The width of the plateau decreases as p_t increases.

The locations on the kinematic boundaries in Figs. 6(a) and 6(b) depend on the value of y_b and m_b which have been taken to be y_N and m_π respectively in the present analysis. Better determination of these quantities using the measured locations of the kinematic boundaries may require more refined measurements of the ridge momentum distribution in many locations in pseudorapidity space.

VIII. EARLY PARTICLE PRODUCTION AT HIGH ENERGIES

The momentum distribution extracted from the near-side ridge data indicates that the early parton rapidity distribution has a plateau structure which extends well into the high rapidity region. The width of the plateau depends on p_t . The greater the value of p_t , the narrower is the width of the plateau. While the evolution scenario of the early rapidity distribution has been outlined in Section VIII of [19], we would like to elaborate in more detail the origin of the rapidity plateau.

It should be kept in mind that the plateau rapidity structure has been known in QCD particle production processes both experimentally and theoretically. In e^+e^- annihilation experiments, the produced particles exhibit a rapidity plateau structure [36, 37, 38, 39, 40]. Many earlier theoretical investigations of QCD particle production processes give a rapidity plateau distribution when a quark pulls away from an anti-quark at high energies [42, 43, 44, 45, 46]. We shall review here the theoretical basis for the occurrence of the rapidity plateau in an elementary particle production process.

As an exact solution of particle production at high energies starting from the first principle of QCD is not available, many phenomenological models have been presented to describe particle production in nucleus-nucleus collisions [56]. Common to many of these models (such as the Lund Model, the Dual Parton Model, the Multiple Collision Model, the ART model, the Lexus Model, the Venus Model, and the Glasma Model, ...) is the elementary particle production process of a color charge pulling away from an anti-color charge at high energies at the early stage of a nucleus-nucleus collision, and the nucleus-nucleus collision consists of many of these elementary production processes.

We can single out one of the elementary production processes for examination and study the particle production process in a model that has many essential features as those in QCD [42, 43, 44, 45, 46]. The model of QED2 [42, 47, 48, 49, 50] are quantum mechanical systems in which a neutral boson exists as a non-perturbative bound state, much as mesons are bound states in QCD. When a positive and negative charge pair are separated in such a system, the vacuum is so polarized that the positive and the negative charges are completely screened, in a manner similar to the confinement of quarks, in which a quark cannot be isolated. It was demonstrated by Casher, Kogut and Susskind [42] in QED2 that the rapidity distribution of produced boson particles in a system of two oppositely charged fermions separating at high relative velocities exhibits a plateau rapidity structure. Such a rapidity plateau structure of produced particles is indeed observed in high-energy $e^+ - e^-$ annihilation experiments as mentioned above [36, 37, 38, 39, 40]. The quark fragmentation function obtained from QED2 [57] agrees with that of Field and Feynman [58] in their phenomenological treatment of QCD strings. These desirable properties of confinement, charge screening, the existence of neutral bound states, and the proper high-energy behavior make it useful for Casher, Kogut, Susskind [42], Bjorken [43] and many others [44, 45, 46] to infer the rapidity plateau structure of produced particles when a color charge recede away from an anti-color charge at high energies.

Previously, a scaling argument was presented to reduce QCD at high energies to an effective two-dimensional field theory by scaling the longitudinal and temporal coordinates by λ and expand the action in power of $1/\lambda$ [59]. We shall try an alternative approach by using the physical argument of transverse confinement to establish the connection between QCD and QED2, in order to study particle production in a quantum mechanical framework.

We consider the elementary particle production process in a flux tube in a nucleus-nucleus collision as a color

charge and an anti-color charge separate from each other at high energies. Produced particles are quanta of the interacting fields. Depending on the environment temperature, they can be considered as partons in the environment of a strongly-coupled quark-gluon plasma and as hadrons in a cold QCD environment at zero temperature. The QCD fields inside the tube consists of the gauge fields and the fermion degrees of freedom. At high energies, the gauge fields can be greatly simplified by noting that the transverse gauge fields A_x and A_y are expected to be proportional to the fermion source transverse velocities, which are smaller as compared to the longitudinal velocity in the z -direction. It is reasonable to ignore the transverse gauge fields A_x , and A_y so that $A_\mu = (A_0, 0, 0, A_z)$ containing only A_0 and A_z degrees of freedom confined in the tube.

The fermion sector can also be approximated. We shall assume that as a result of the non-perturbative non-Abelian gauge interaction, transverse confinement is established, and this confinement can be conveniently described by a scalar potential $m(r)$ that limits the amplitude of the fermions to the region around the flux tube, as in previous descriptions [55, 60, 61, 62, 63]. The Dirac equation for a fermion in the tube in cylindrical coordinates (r, φ, z) is:

$$\{\gamma^\mu(\pi_\mu - eA_\mu) - m(r)\} \Psi(r, \varphi, z, t) = 0. \quad (33)$$

Following the results of Ref. [60, 63], we seek a solution of the Dirac equation (33) in the form

$$\Psi(r, \varphi, z, t) = \left[\gamma^\mu(\pi_\mu - eA_\mu) + m(r) \right] \psi(r, \varphi, z, t). \quad (34)$$

The equation for ψ is

$$\left\{ (p_0 - eA_0)^2 - (p_z - eA_z)^2 + i\alpha^3 e(\partial_z A_0 - \partial_0 A_z) + \mathbf{p}_\perp^2 - m^2(r) + i \left[(\gamma^1 \partial_1 + \gamma^2 \partial_2) m(r) \right] \right\} \psi(r, \varphi, z, t) = 0, \quad (35)$$

where e is the coupling constant. We note that $[\alpha^3, J_z] = 0$, where $J_z = -i\partial/\partial\phi + \sigma_z/2$ is the third component of the angular momentum operator. Furthermore, both J_z and α^3 commute with the operator acting on $\psi(r, \phi, z, t)$ in Eq. (35). Upon using the representation in Ref. [60], the eigenfunction of α^3 satisfying $\alpha^3 \mu_\lambda = \eta_\lambda \mu_\lambda$ are

$$\mu_1 = \frac{1}{\sqrt{2}} \begin{pmatrix} 1 \\ 0 \\ 1 \\ 0 \end{pmatrix}, \quad \mu_2 = \frac{1}{\sqrt{2}} \begin{pmatrix} 0 \\ 1 \\ 0 \\ -1 \end{pmatrix}, \quad \mu_3 = \frac{1}{\sqrt{2}} \begin{pmatrix} 1 \\ 0 \\ -1 \\ 0 \end{pmatrix}, \quad \mu_4 = \frac{1}{\sqrt{2}} \begin{pmatrix} 0 \\ 1 \\ 0 \\ 1 \end{pmatrix}, \quad (36)$$

with $\eta_{1,2} = +1$ and with $\eta_{3,4} = -1$. Therefore, we may choose $\psi(r, \varphi, z, t)$ to be factorized as

$$\psi_{J_z}(r, \varphi, z, t) = \sum_{\eta=-1,1} f_{J_z \eta}(z, t) R_{J_z \eta}(r, \varphi), \quad (37)$$

with $R_{J_z \eta}(r, \varphi)$ to be simultaneous eigenfunctions of J_z and α^3 . The eigenfunctions of J_z satisfying $J_z R_{J_z \eta} = (\nu + \sigma_z/2) R_{J_z \eta}$ are

$$R_{J_z \ 1}(r, \phi) = g_{1\nu}(r) e^{i\nu\phi} \mu_1 - g_{2\nu}(r) e^{i(\nu+1)\phi} \mu_2, \quad (38)$$

$$R_{J_z -1} = g_{1\nu}(r) e^{i\nu\phi} \mu_3 + g_{2\nu}(r) e^{i(\nu+1)\phi} \mu_4. \quad (39)$$

As a result of the transverse confinement, the gauge fields A_0 and A_z are confined within the transverse dimensions of the flux tube. For high-energy collisions, the transverse dimensions of the flux tube are much smaller than the longitudinal dimension. To study the dynamics along the longitudinal direction, it is reasonable to average the gauge fields A_0 and A_z over the transverse profile of the flux tube. After such a transverse averaging, the dynamics of A_0 and A_z along the longitudinal direction can be approximated to be independent of the transverse coordinates. One can then use the method of the separation of variables to separate the equation of motion. By introducing the transverse eigenvalue m_\perp , the Dirac equation can be separated into the set of equations in different coordinates,

$$[p_0 - A_0(z, t)]^2 - [p_z - eA_z(z, t)]^2 - m_\perp^2 - \eta i e [\partial_z A_0(z, t) - \partial_0 A_z(z, t)] f_{J_z \eta}(z, t) = 0, \quad (40)$$

$$\left[\mathbf{p}_\perp^2(\nu) + m^2(r) - m_\perp^2 \right] g_{1\nu}(r) = i \frac{\partial m(r)}{\partial r} g_{2\nu}(r), \quad (41)$$

$$\left[\mathbf{p}_\perp^2(\nu + 1) + m^2(r) - m_\perp^2 \right] g_{2\nu}(r) = -i \frac{\partial m(r)}{\partial r} g_{1\nu}(r), \quad (42)$$

where

$$\mathbf{p}_\perp^2(\nu) = -\frac{1}{r} \frac{\partial}{\partial r} \left(r \frac{\partial}{\partial r} \right) + \frac{\nu^2}{r^2}. \quad (43)$$

Here, m_\perp is the eigenvalue for the coupled transverse equations (41), and (42), obtained by imposing the boundary condition that the transverse wave functions $g_{1\nu}$ and $g_{2\nu}$ are transversely confined with a vanishing probability at $r \rightarrow \infty$. The eigenvalue m_\perp depends on J_z and is independent of the quantum number η . Some examples of $m(r)$, m_\perp and transverse wave functions have been presented previously [55, 62, 63].

We can write the wave function ψ with the quantum number J_z and a mass m_\perp as a two-component wave function in an abstract two-dimensional QED2 space as

$$\psi_{\text{qed2}} = \begin{pmatrix} f_{J_z 1} \\ f_{J_z -1} \end{pmatrix}. \quad (44)$$

In terms of this wave function, Eq. (40) becomes

$$\left[\gamma_{\text{qed2}}^0 [p_0 - eA_0(x^1, t)] + \gamma_{\text{qed2}}^1 [p_1 - eA_1(x^1, t)] - m_\perp \right] \psi_{\text{qed2}}(x^1, t) = 0, \quad (45)$$

where we re-label the longitudinal z -axis as the x^1 -axis in QED2, and

$$\gamma_{\text{qed2}}^0 = \begin{pmatrix} 0 & 1 \\ 1 & 0 \end{pmatrix}, \quad (46)$$

$$\gamma_{\text{qed2}}^1 = i\sigma_2 = \begin{pmatrix} 0 & 1 \\ -1 & 0 \end{pmatrix}. \quad (47)$$

For brevity of notation, the subscript ‘qed2’ will be omitted. It should be kept in mind that the transverse state with J_z in different transverse excitations correspond to QED2 with different m_\perp . We shall be interested in the state with the lowest m_\perp .

The above discussions shows how the fermion and the gauge field in QCD4 in a flux tube can be approximately mapped into elements in QED2 for high-energy processes. Although the non-Abelian nature of the gauge field in QCD is needed to lead to the formation of the confining flux tube, the non-Abelian property is not needed for particle production in QED2 at high-energies. An Abelian QED2 field theory possesses the desirable properties of confinement and charge screening, and it suffices to describe the particle production process at high energies. Furthermore, in the non-Abelian field tensor

$$F_{01}^i = \partial_0 A_1^i - \partial_1 A_0^i + g f^{ijk} A_0^j A_1^k, \quad (48)$$

the non-linear quadratic term contains the product of A_0^j and A_1^k . One can convenient choose the Coulomb gauge $A_1^k = 0$ such that the non-linear quadratic term does not contribute. We can therefore ignore the non-Abelian nature of the gauge fields and approximate them to be

$$F_{\mu\nu} = \partial_\mu A_\nu - \partial_\nu A_\mu, \quad (49)$$

where $\mu, \nu = 0, 1$. The fermions give rise to the current

$$j^\mu = e \bar{\psi} \gamma^\mu \psi, \quad (50)$$

which generates the gauge fields according to

$$\partial_\nu F^{\mu\nu} = -j^\mu. \quad (51)$$

Eqs. (45), (49), and (51) constitute the equations for the quantum mechanical system of QED2 with a fermion of mass m_\perp . Thus, by assuming QCD confined within a flux tube, the longitudinal dynamics of the system can be approximated as those of QED2 with a mass m_\perp . The gauge fields A^μ ($\mu = 0, 1$) depend on the fermion field ψ . The fermion field ψ , in turn, depends on the gauge field A^μ . The coupling is quite complicated and leads to a non-linear problem of great complexity. Remarkably, Schwinger found that QED2 involving massless fermions with the gauge interaction is equivalent to a free boson field ϕ with a mass $\mu_0 = e/\sqrt{\pi}$, where e is the coupling constant [47].

IX. PARTICLE PRODUCTION AS AN INITIAL-VALUE PROBLEM IN BOSONIZED QED2

In mapping elements of QCD4 approximately into elements of massive QED2, what is the relationship between the coupling constant g in QCD4 and the coupling constant e in QED2? By limiting the motion and the source distribution to reside in the longitudinal direction, the coupling constant e in QED2 acquire the dimension of a mass. The confinement property is a non-perturbative property of QCD4. The coupling constant e in QED2 should therefore be non-perturbatively related to g . The relationship can be retrieved by comparing non-perturbative quantities. In QED2 with the Coulomb gauge $A_1 = 0$, the interaction energy between a quark and an anti-quark separated at a separation of x is $e^2 A_0(x) = e^2 x/2$. On the other hand, in QCD4, the non-perturbative confining interaction energy between a quark and an anti-quark is bx where b is the string tension. Therefore, equating the two interaction energies, we find a relation between e in QED2 and the non-perturbative string tension b in QCD4,

$$e = \sqrt{2b}. \quad (52)$$

If we take the string tension to be $b = 1$ GeV/fm, then $e = 0.628$ GeV. The boson mass in massless QED2 is $\mu_0 = e/\sqrt{\pi} = 0.354$ GeV.

The case of massive QED2 with a fermion mass m_\perp can be studied by bosonization. It is equivalent to the system of free bosons of mass μ_0 interacting with an interaction that depends on m_\perp [49, 50]. Does QCD corresponds to the case of strong coupling with $e \gg m_\perp$, or the case weak coupling with $e \ll m_\perp$? The case of strong coupling is characterized by a quasi-free bosons with confining fermions and charge screening, while the limit of weak coupling approaches free Dirac theory with almost free fermions dressed up as bosons having a mass close to the free fermion rest mass [50].

We can estimate m_\perp to be of the order of $\hbar/(\text{tube radius})$ where the flux tube radius is of order 1 fm, leading to $m_\perp \sim 0.2$ GeV. We have $\mu_0 \gg m_\perp$ which correspond to the case of strong coupling with fermion confinement and color-charge screening, rather than quasi-free Dirac particles. Accordingly, the mass-perturbation theory can be used to discuss the particle production process in our case of massive QED2.

In the mass-perturbation theory, the unperturbed theory is massless QED2 and the mass m_\perp is treated as a perturbation. Up to the second order in m_\perp , the mass perturbation theory gives a quasi-free boson with a mass M given by [64]

$$M^2 = \mu_0^2 + 2e^\gamma \mu_0 m_\perp + 1.0678 e^{2\gamma} m_\perp^2, \quad (53)$$

where $\gamma = 0.5772$ is the Euler constant. We therefore have $M \sim \mu_0 + e^\gamma m_\perp$. For our case of $\mu_0 = 0.354$ GeV and $m_\perp \sim 0.2$ GeV, we get $M \sim 0.71$ GeV, which comes close to the spin-spin averaged mass of 0.62 GeV for the π - ρ pair. Thus, the boson of massive QED2 finds its correspondence as the boson in QCD that splits into π and ρ when the spin-spin interaction is taken into account.

As mass perturbation theory is based on massless QED2 with m_\perp as a perturbation, the application of the theory to particle production process involves in using the results of massless QED2 and replacing the boson mass μ_0 in these massless QED2 results by the corrected mass M . In practical applications, this amounts to replacing μ_0 with the physical mass, including the effects of the effective mass increase due to the transverse momentum. As pions are the most predominantly produced particle, the phenomenological treatment then involves in replacing μ_0 by $M = \sqrt{m_\pi^2 + p_{\perp,\pi}^2}$.

We can review the rapidity distribution for massless QED2 obtained previously [63]. The relation between the bosonic and the fermionic quantities in massless QED2 is [42, 49, 50]

$$j^\mu = -e\epsilon^{\mu\nu} \partial_\nu \phi / \sqrt{\pi}, \quad (54)$$

where j^μ is the fermionic current which can be taken to be a real quantity, and $\epsilon^{\mu\nu}$ is the antisymmetric tensor $\epsilon^{01} = -\epsilon_{01} = -1$. We note that, as j^μ is a vector field and $\epsilon^{\mu\nu}$ is a pseudotensor, the field ϕ is a real pseudoscalar field, and it represents the color electric field F^{01} , as $F^{01} = e\phi/\sqrt{\pi}$. If the current j^μ arising from the fermions is initially known, then the dynamics of the pseudoscalar field ϕ can be inferred at all times. Treating the problem as a system of quasi-free bosons with a mass M , the initial value conditions will allow us to determine the dynamics of the system. To apply the results to our case, we will work within mass perturbation theory which is a quasi-free boson system with $e/\sqrt{\pi}$ replaced by M .

Given an initial fermion charge distribution $j_\mu(x, t = 0)$, its Fourier transform is $\tilde{j}^\mu(p^1)$ is

$$\tilde{j}^\mu(p^1) = \frac{1}{\sqrt{2\pi}} \int dx e^{-ip^1 x} j^\mu(x, 0). \quad (55)$$

We show previously [44] that the momentum distribution of the bosons is then given by

$$\frac{dN}{dp^1} = \frac{\pi}{2p^0 e^2} \left[\frac{p^0}{p^1} \tilde{j}^0(p^1) + \tilde{j}^1(p^1) \right] \left[\frac{p^0}{p^1} \tilde{j}^0(-p^1) + \tilde{j}^1(-p^1) \right], \quad (56)$$

and the rapidity distribution of the produced particles is

$$\frac{dN}{dy} = \frac{\pi}{2e^2} \left[\frac{p^0}{p^1} \tilde{j}^0(p^1) + \tilde{j}^1(p^1) \right] \left[\frac{p^0}{p^1} \tilde{j}^0(-p^1) + \tilde{j}^1(-p^1) \right]. \quad (57)$$

This gives a simple relation between the rapidity distribution and the Fourier transforms of the initial fermionic charge current.

We can review how this initial-value problem in massless QED2 can be formulated for the case of a positive charge νe separating from a negative charge $-\nu e$ with a center-of-mass energy \sqrt{s} [44]. We work in the center-of-mass system and start at $t = 0$ with the charge and anti-charge pair superimposed so that the total charge density of the system at $t = 0$ is zero:

$$j^0(x, 0) = 0. \quad (58)$$

To construct the initial longitudinal current, we introduce a distribution that depend on σ .

$$j^1(x, t) = \frac{\partial}{\partial t} \left\{ \frac{\nu}{2} [\tanh((x+t)/\sigma) + 1] + \frac{\nu}{2} [\tanh((x-t)/\sigma) + 1] \right\}. \quad (59)$$

In this case, the initial current which arises from a charge νe moving in the positive x direction and another charge $-\nu e$ moving in the negative x direction is given by

$$j^1(x, 0) = \frac{\nu e}{\sigma \cosh^2(x/\sigma)}. \quad (60)$$

In the limit as σ approaches zero, the above current is proportional to a delta function. The diffusivity σ is related to the total invariant mass \sqrt{s} of the system; using the energy $P^0 = \sqrt{s}$ at the initial time $t = 0$, we obtain a relation between σ and \sqrt{s} :

$$\sigma = \frac{2\pi\nu^2}{3\sqrt{s}}. \quad (61)$$

For this current distribution $j^\mu(x, 0)$ the Fourier transform of $j^1(x, 0)$ is

$$\tilde{j}^1(p^1) = \frac{\nu e \pi p^1 \sigma}{\sqrt{2\pi} \sinh(\pi p^1 \sigma / 2)}, \quad (62)$$

and the rapidity distribution in massless QED2 is [44]

$$\frac{dN}{dy} = \frac{\nu^2 \xi^2}{\sinh^2 \xi}, \quad (63)$$

where

$$\xi = \frac{\nu^2 \pi^2 \mu_0 \sinh y}{3\sqrt{s}}. \quad (64)$$

The rapidity distribution therefore shows a plateau structure around $y \sim 0$. In the limit of very high energy, the rapidity distribution is $dN/dy = \nu^2$, which agrees with the result of Casher [42] (for $\nu = 1$).

Within the mass perturbation theory, we can approximate the particle production process of massive QED2 using the results from massless QED2 and replacing the μ_0 of massless QED2 in Eq. (64) by M in massive QED2, with the result

$$\xi = \frac{\nu^2 \pi^2 M \sinh y}{3\sqrt{s}}. \quad (65)$$

Using Eqs. (63) and (65) by replacing μ_0 with the phenomenological mass $M = \sqrt{m_\pi^2 + \langle p_{\perp, \pi} \rangle^2} = 0.30$ GeV and $\nu = 2.45$ gives a good phenomenological fit to the dN_{π^\pm}/dy data in e^+e^- experiment at $\sqrt{s} = 29$ GeV (in Fig. (40) of [36]).

X. EVOLUTION OF THE MEDIUM PARTON MOMENTUM DISTRIBUTION

We conclude from our discussions in the last two sections that in addition to experimental evidences for the rapidity plateau in elementary QCD particle production processes, theoretical investigations in plausible models also show the occurrence of a rapidity plateau when a color charge pulls away from an anti-color charge at high energies. As a nucleus-nucleus consists of elementary production processes of string fragmentation, there can be a similar plateau structure in the rapidity distribution of the produced medium partons, consistent with the parton rapidity plateau we have extracted at the early stage of the nucleus-nucleus collision.

In nucleus-nucleus collisions, this early parton momentum distribution can be probed by a jet produced in the early stage of the collision. Those medium partons kicked by the jet subsequently materialize as ridge particles and they retain the property of the rapidity plateau.

The plateau rapidity structure of the early parton momentum distribution differ from the Gaussian rapidity distribution of the bulk matter [65, 66, 67]. How does one understand such a difference?

It is important to point out that the early momentum distribution represents the momentum distribution at the early stage of the nucleus-nucleus collision as it involves the direct reaction with the jet, which occurs only at the early stage of the nucleus-nucleus collision. On the other hand, the momentum distribution of the bulk matter represent the momentum distribution of the bulk matter at the end-point of the nucleus-nucleus collision. A considerable period of time separates the beginning, early stage of the nucleus-nucleus collision and the end-point of the nucleus-nucleus collision. Significant dynamical evolution must have occurred between these two separate time points, as described schematically in Fig. 9 of Ref. [19]. The time evolution of the momentum distribution will make the end-point momentum distribution of the bulk matter different from the early parton momentum distribution.

Evidence for the occurrence of a dynamical evolution of the momentum distribution presents itself in the difference of (i) the transverse momentum distribution extracted at the moment of the jet-(medium parton) collisions, and (ii) the transverse momentum distribution of the bulk matter at the end-point of the nucleus-nucleus collision. The extracted early parton transverse momentum distribution, as given by Eqs. (19), and (32), has a thermal-like distributions, with an initial inverse slope $T = 0.5$ GeV that is slightly greater than the inverse slope of the end-point transverse momentum distribution, consistent with the direction of transverse momentum evolution from a higher inverse slope T to a lower inverse slope T value [7]. We expect that the rapidity distribution will likewise evolve and its shape will change with time. There is no reason to expect that the longitudinal momentum distribution at the early stage of the nucleus-nucleus collision should be the same as the corresponding longitudinal momentum distribution at the end-point of the nucleus-nucleus collision.

To understand the evolution of the medium parton momentum distributions, we should think of the full momentum distribution to be a six-dimension distribution function $F(\mathbf{r}, \mathbf{p}, t)$ of the medium that depends both on the spatial and momentum coordinates, as well as on the lapsed time t . The parton momentum distribution extracted here is in effect an average of this the six-dimensional distribution function F over spatial and temporal coordinates of the collision points in the early stage of the nucleus-nucleus collision, using the jet as a probe. After the early stage of jet-(medium parton) collisions, partons from one position will collide with partons of adjacent positions. These collisions will modify the momenta of the colliding partons, leading to a change of the distribution function $F(\mathbf{r}, \mathbf{p}, t)$ as a function of time. How the evolution will take place is a problem of great complexity that depends on models with many unknown theoretical elements [56]. Nevertheless, one expects that starting with a non-isotropic plateau rapidity distribution that is much elongated in the longitudinal direction, a collision of two partons with large and opposing longitudinal momenta in adjacent spatial locations will redistribute the partons from the longitudinal direction towards the transverse directions, with a decrease in the longitudinal momenta of the colliding partons. Hence, the evolution will smooth out the anisotropic plateau rapidity structure to a significant degree as time proceeds.

XI. DEPENDENCE OF THE FRAGMENTATION FUNCTION ON THE JET-(MEDIUM PARTON) COLLISION NUMBER

We turn now to investigate the geometry-dependent part of the ridge and trigger particle yields, as given previously in Eqs. (7), (14), and (15). The jet fragmentation function in these equations depends on the number of collisions N (or N_k) suffered by the jet parton, and the observed physical quantities depend on the distribution $P(N)$. We envisage jet partons to be produced by binary nucleon-nucleon hard-scattering processes and we focus our attention on one of the jet partons. We consider the jet parton to occur at $\eta_{\text{jet}} = 0$ such that the jet momentum \mathbf{p}_j , the trigger particle momentum \mathbf{p}_{trig} , and the momentum kick \mathbf{q} all lie in the mid-rapidity transverse plane in the collider system, pointing in the same direction. The vector symbol for these quantities can be understood.

We envisage that in the passage of the parent jet parton in the dense medium, the jet parton with initial momentum p_j imparts a momentum q to each kicked medium parton, and loses a momentum Nq after N jet-(medium parton)

collisions. In addition to collisional momentum loss, the jet parton can lose momentum by gluon radiation [51]. As the radiated gluon will likely come out in a cone along the jet direction in random azimuthal angles, the average momentum loss due to gluon radiation $\langle \Delta_r \rangle$ lies along the jet direction \mathbf{e}_j . We can parametrize the radiative gluon momentum loss phenomenologically by $|\Delta_r| = Nq_r$ where the q_r value obtained from experimental data will need to be compared with theoretical models. In practice, the collisional and radiative momentum losses appear together as the sum total $(q + q_r)$ in the fragmentation function [Eq. (71)]. Furthermore, there can be additional attenuation ζ_a due to absorptive inelastic processes of removing the jet from the jet channel. Only the sum of the absorptive, collisional, and radiative contributions, leading to the total attenuation coefficient ζ , can be obtained by comparison with experimental jet quenching data [Eqs. (73) and (75)].

Upon including the momentum loss due to jet-(medium parton) collisions and gluon radiation in the momentum kick model, Eq. (7) becomes

$$N_{\text{trig}} = \int d\mathbf{p}_j \frac{dN_j}{d\mathbf{p}_j} \sum_{N=0}^{N_{\text{max}}} P(N) e^{-\zeta_a N} D(p_{\text{trig}}; p_j - N(q + q_r)). \quad (66)$$

We wish to write out the dependence of the fragmentation function D on N in the above equation explicitly. The dominant contribution of the jet production process comes from gluon-gluon collisions [68]. The relevant fragmentation function of fragmenting a pion out of a gluon at the momentum scale Q_0^2 , can be written in the form [68]

$$zD(z, Q_0^2) \sim C_\pi (1 - z)^{a_1}, \quad (67)$$

where $z = p_{\text{trig}}/p_j$ and C_π is a constant. In perturbative QCD, the fragmentation function near $z = 1$ varies with the QCD momentum scale Q according to [68, 69]

$$zD(z, Q^2) \simeq zD(z, Q_0^2) e^{0.69G\bar{s}(-\ln z)^{4G\bar{s}}} \frac{\Gamma(a_1 + 1)}{\Gamma(a_1 + 1 + 4G\bar{s})}, \quad (68)$$

where $G = 4/25$, and $\bar{s} = \ln[\ln(Q^2/\Lambda^2)/\ln(Q_0^2/\Lambda^2)]$. After the jet suffers N jet-(medium parton) collisions with the medium partons, the fragmentation function for a pion to fragment out of the final jet of momentum $z_N = p_{\text{trig}}/[p_j - N(q + q_r)]$ is

$$D(z_N, Q^2) = C_\pi e^{0.69G\bar{s}} \exp\{-\ln z_N + a_1 \ln(1 - z_N) + 4G\bar{s} \ln[(-\ln z_N)]\} \frac{\Gamma(a_1 + 1)}{\Gamma(a_1 + 1 + 4G\bar{s})}. \quad (69)$$

Upon expanding the exponent index of the above function in power of $N(q + q_r)/p_j$ and retaining the term first order in $N(q + q_r)/p_j$, we obtain the dependence of the jet fragmentation function on the jet-(medium parton) collision number N ,

$$D(p_{\text{trig}}/(p_j - N(q + q_r)), Q^2) \simeq D(p_{\text{trig}}/p_j, Q^2) e^{-\zeta_D N}, \quad (70)$$

where

$$\zeta_D = \left(\frac{1}{p_{\text{trig}}/p_j} + \frac{a_1}{1 - p_{\text{trig}}/p_j} + \frac{4G\bar{s}}{\ln(p_j/p_{\text{trig}})} \frac{p_j}{p_{\text{trig}}} \right) \frac{p_{\text{trig}}(q + q_r)}{p_j^2}. \quad (71)$$

Substituting this relationship into Eq. (66), we get

$$N_{\text{trig}} = \int d\mathbf{p}_j \frac{dN_j}{d\mathbf{p}_j} D(\mathbf{p}_{\text{trig}}; \mathbf{p}_j) \sum_{N=0}^{N_{\text{max}}} P(N) e^{-\zeta N}, \quad (72)$$

where we have combined ζ_a with ζ_D ,

$$\zeta = \zeta_a + \zeta_D. \quad (73)$$

Because of the normalization condition Eq. (5) for the fragmentation function and the definition of $dN_j/d\mathbf{p}_j$ in Eq. (1), we obtain

$$N_{\text{trig}} = N_{\text{bin}} \sum_{N=0}^{N_{\text{max}}} P(N) e^{-\zeta N}, \quad (74)$$

and we get the jet quenching measure

$$R_{AA} = \frac{N_{\text{trig}}}{N_{\text{bin}}} = \sum_{N=0}^{N_{\text{max}}} P(N) e^{-\zeta N}, \quad (75)$$

and the average number of jet-(medium parton) collisions per trigger

$$\langle N \rangle = \langle N_k \rangle = \sum_{N=1}^{N_{\text{max}}} N P(N) e^{-\zeta N} / \sum_{N=0}^{N_{\text{max}}} P(N) e^{-\zeta N}. \quad (76)$$

The presence of the attenuation factor $e^{-\zeta N}$ implies that detected trigger particles are likely to originate near the surface where the number of jet-(medium parton) collisions N is smallest. The quantity ζ_a is not known. The quantity ζ_D depends on $q + q_r$ and p_j . We can estimate the contribution of collisional contribution to the value of ζ_D by inferring the approximate average value of p_j for $p_{\text{trig}} \sim 5$ GeV. As $p_j \sim (p_{\text{trig}} + \langle N \rangle q + 3N_{\text{jet}} T_{\text{jet}})$ with $\langle N \rangle \sim 6$, $q \sim 1$ GeV, $N_{\text{jet}} = 0.75$, $T_{\text{jet}} = 0.55$ GeV, we estimate that $p_j \sim 2.5 p_{\text{trig}}$. If we use $Q^2 = p_j^2$, $Q_0^2 = 3$ GeV², $a_1 = 1.5$ and $\Lambda = 0.5$ GeV as in [68] we can use Eq. (71) and estimate the contribution to ζ_D from q to be approximately 0.22. There can be additional contributions from the radiative energy loss q_r . We shall set ζ as a free parameter to describe the experimental R_{AA} data by searching for ζ around the neighborhood of about 0.22. We find in Section XIII that the experimental jet quenching and ridge yield data are consistent with a value of $\zeta = 0.20$ which comes very close to the value of 0.22 estimated here.

XII. GEOMETRY DEPENDENCE OF TRIGGER AND RIDGE YIELDS

Because the ridge particle yield has been measured on the basis of the yield per trigger particle, it is necessary to determine the trigger yield N_{trig} as a function of the geometrical variables, in addition to determining the number of ridge particles. The trigger particle yield is quenched due to the energy loss of the jet parton. We therefore need to study jet quenching and follow the trajectory of the jet.

From our earlier considerations, the relevant physical quantities are given in terms of N , the number of medium partons kicked by the jet on its way to emerge from the medium. This quantity N , in turn, is equal to the number of jet-(medium parton) collisions N_k suffered by the jet parton. We assume for simplicity that the energetic jet parton travels along a straight line trajectory with a velocity nearly the speed of light, making an angle ϕ_s with respect to the reaction plane, $\phi_s = \phi_{\text{jet}} - \phi_{\text{RP}}$. Using the mid-point O between the centers of the two nuclei as the origin, we set up a transverse coordinate system for the jet source point \mathbf{b}_0 and the jet trajectory point \mathbf{b}' as shown in Fig. 7.

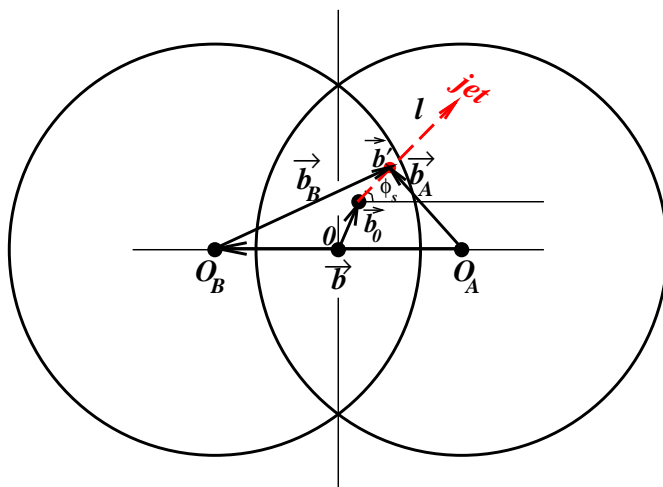


FIG. 7: (Color online) The transverse coordinate system used for the jet source point \mathbf{b}_0 and the trajectory point \mathbf{b}' . The coordinate origin is located at the midpoint O between the two colliding nuclei, whose centers are located at O_A and O_B separated by an impact parameter \mathbf{b} . The jet trajectory lies along l and makes an angle ϕ_s with respect to the reaction plane.

We consider the jet source point at \mathbf{b}_0 , from which a mid-rapidity jet parton originates. The number of jet-(medium

parton) collisions along the jet trajectory making an angle ϕ_s with respect to the reaction plane is

$$N_k(\mathbf{b}_0, \phi_s) = \int_0^\infty \sigma dl \frac{dN_{\text{parton}}}{dV} [\mathbf{b}'(\mathbf{b}_0, \phi_s)], \quad (77)$$

where $0 < l < \infty$ parametrizes the jet trajectory, σ is the jet-(medium parton) scattering cross section, and $dN_{\text{parton}}(\mathbf{b}')/dV$ is the parton density of the medium at \mathbf{b}' along the trajectory l . Jet-(medium parton) collisions take place along different parts of the trajectory at different l and involve the medium at different stages of the expansion. They depend on the space-time dynamics of the jet and the medium. To follow the jet-(medium parton) collisions along the jet trajectory, we need a time clock to track the coordinates of the jet and the motion of the medium. We start the time clock for time measurement at the moment of maximum overlap of the colliding nuclei, and the jet is produced by nucleon-nucleon collisions at a time $t \sim \hbar/(10\text{GeV})$ which can be taken to be ~ 0 . The trajectory path length l is then a measure of the time coordinate, $t \approx l$, which is needed to follow the longitudinal and transverse expansions of the medium.

The trajectory point \mathbf{b}' depends on the jet source origin point \mathbf{b}_0 and the jet azimuthal angle ϕ_s as

$$\mathbf{b}'(\mathbf{b}_0, \phi_s) = (b'_x, b'_y) = (b_{0x} + l \cos \phi_s, b_{0y} + l \sin \phi_s). \quad (78)$$

If we approximately represent the modification of the density arising from longitudinal and transverse expansion by an effective time parameter τ_{eff} using the initial parton density in the following approximation,

$$N_k(\mathbf{b}_0, \phi_s) = \frac{\sigma}{\tau_{\text{eff}}} \int_0^\infty dl \frac{dN_{\text{parton}}}{d\mathbf{b}'} [\mathbf{b}'(\mathbf{b}_0, \phi_s)]. \quad (79)$$

then we find that the data can be described by $\zeta = 0.22$ and $\sigma/\tau_{\text{eff}} \sim 0.025$ fm. Such a picture only gives a rather crude description of the path-length dependence of the ridge yield.

In order to give a more realistic picture, we describe the medium by an expanding fluid with an initial density given by the distribution of the participants at the moment of maximum nuclear overlap. We assume that the longitudinal expansion begins at the moment of maximum overlap as the initial momenta are directed along the longitudinal direction. A period of time t_0 is however needed to convert the longitudinal kinetic energy into entropy to produce particles with a transverse mass. The transverse hydrodynamical expansion can then commence at $t \geq t_0$. The time for producing a particle with a typical transverse mass of about 0.35 GeV is $\hbar/(0.35 \text{ GeV}) \sim 0.6$ fm/c, which is also the time estimated for the thermalization of the produced matter [70]. We therefore take $t_0 = 0.6$ fm/c.

As we will focus our attention in the mid-rapidity region where experimental data are available, Bjorken hydrodynamics [43] and Landau hydrodynamics [71, 72] coincide [73, 74] and we can use Bjorken hydrodynamics to describe the longitudinal expansion. For a hydrodynamical system undergoing Bjorken longitudinal expansion, the transverse expansion can be described by the hydrodynamical solution of Baym *et al.* [75]. Using the method of characteristics, they find that the energy density and velocity field in the transverse direction can be described well approximately by analytic formulas.

Accordingly, we follow the jet along its trajectory at l specified by the trajectory point \mathbf{b}' with a transverse magnitude $b' = |\mathbf{b}'|$ (measured from the origin O) at at time $t = l$. The time after the onset of the transverse expansion is then $t_R = t - t_0$, and a rarefaction wave travels from the transverse radius R inward with the speed of sound c_s . The dynamics is different whether the rarefaction wave has reached this medium point b' or not. The transverse space of the medium can be divided into Region I and II.

In Region I characterized by $b' < R - c_s t_R$, the rarefaction wave has not reached this medium point at \mathbf{b}' . In this region, the medium has not started to expand transversely with transverse velocity $v_\perp = 0$ while the longitudinal expansion has already commenced. Due to the longitudinal expansion the density is depleted and the temperature is decreased as [75]

$$T \propto (t_0/t)^{c_s^2}. \quad (80)$$

As the entropy density and number and entropy densities are proportional to T^{1/c_s^2} , we have

$$\frac{dN_{\text{parton}}}{dV}(b', t) = \frac{dN_{\text{parton}}}{dV}(b'_{\text{init}}, t = t_0) \frac{t_0}{t}, \quad (81)$$

with $b'_{\text{init}} = b'$ in Region I.

In Region II defined by $R - c_s t_R < b' < R + t_R$, where the inward-traveling rarefaction wave has passed through already. The medium is expanding transversely outward and the transverse velocity v_\perp at the point \mathbf{b}' at the time t is

$$v_\perp = \frac{b' - R + c_s t_R}{t_R + c_s(b' - R)}. \quad (82)$$

The transverse velocity v_\perp is unity (speed of light) at the surface point $R + t_R$, and is zero at the point $b' - c_s t_R$ where the rarefaction wave has just arrived. The medium temperature in this region is given by [75]

$$T(b', t) = T_0(b'_{\text{init}}, t = t_0) \left(\frac{t_R - b' + R}{t_R + b' - R} \frac{1 - c_s}{1 + c_s} \right)^{c_s/2} \left(\frac{t_0}{t} \right)^d, \quad (83)$$

where $b'_{\text{init}} = b' - v_\perp t_R$ is the initial position that reaches b' at t_R , and if $b' - v_\perp t_R \leq 0$ we set $b'_{\text{init}} = 0$. Here the exponential index d is [75]

$$d = \frac{c_s^2}{2} \left[1 + \frac{1}{1 - v_\perp(b', t)c_s} \right]. \quad (84)$$

The corresponding medium number density in the coordinate frame in which the trajectory l is measured (Fig. 7) is therefore

$$\frac{dN_{\text{parton}}}{dV}(b', t) = \gamma \frac{dN_{\text{parton}}}{dV}(b'_{\text{init}}, t = t_0) \left(\frac{t_R - b' + R}{t_R + b' - R} \frac{1 - c_s}{1 + c_s} \right)^{1/2 c_s} \left(\frac{t_0}{t} \right)^{d/c_s^2}, \quad (85)$$

where

$$\gamma = \frac{1}{\sqrt{1 - v_\perp^2}}, \quad (86)$$

and γ is to take into account the change in the medium number density due to the flow velocity of the medium along the transverse direction. While the boundary R is independent of the azimuthal angle of \mathbf{b}' for the central collision, the boundary radius is a function of the azimuthal angle for non-central collisions. We shall assume that the relations between the density and the radius given above remain applicable by using a radius R that depends on the azimuthal angle. These results of the number density at various transverse points allow one to obtain the absorption exponent index for a jet to pass through an expanding medium. In numerical calculations, we take the speed of sound to be $c_s = 1/\sqrt{3}$.

The medium parton density dN_{parton}/dV at $(b'_{\text{init}}, t = t_0)$ is related to the parton transverse density $dN_{\text{parton}}/d\mathbf{b}'$ at t_0 by

$$\frac{dN_{\text{parton}}}{dV}(b'_{\text{init}}, t = t_0) = \frac{dN_{\text{parton}}}{2t_0 d\mathbf{b}'}(b'_{\text{init}}, t = t_0) \quad (87)$$

We can relate the initial parton number transverse density $dN_{\text{parton}}/d\mathbf{b}'$ at $t = t_0$ to the corresponding participant initial number transverse density $dN_{\text{part}}/d\mathbf{b}'$ as

$$\frac{dN_{\text{parton}}}{d\mathbf{b}'} = \frac{dN_{\text{parton}}}{dN_{\text{part}}} \frac{dN_{\text{part}}}{d\mathbf{b}'} = \kappa \frac{dN_{\text{part}}}{d\mathbf{b}'}, \quad (88)$$

where $\kappa = dN_{\text{parton}}/dN_{\text{part}}$ is the number of partons per participant. A previous collection of data gives $N_{\text{ch}}/\langle N_{\text{part}}/2 \rangle = 28$ for $\sqrt{s_{NN}} = 200$ GeV and 16 for $\sqrt{s_{NN}} = 62$ GeV (see [76, 77]). If we use the parton-hadron duality and count the parton number by (3/2) times the charged multiplicity of detected hadrons, then we get

$$\kappa = \begin{cases} 21 & \text{for } \sqrt{s_{NN}} = 200 \text{ GeV} \\ 12 & \text{for } \sqrt{s_{NN}} = 62 \text{ GeV.} \end{cases} \quad (89)$$

A given source point \mathbf{b}_0 and a given azimuthal angle ϕ_s will lead to $N_k(\mathbf{b}_0, \phi_s)$ number of kicked medium partons, which we shall identify by parton-hadron duality as ridge particles. The jet number transverse density is given by the binary nucleon-nucleon collision number transverse density, as nucleon-nucleon collisions are the source of jets. We need to weight the number of kicked medium particles by the local binary collision number element $d\mathbf{b}_0 \times dN_{\text{bin}}/d\mathbf{b}_0$. The normalized probability distribution $P(N, \phi_s)$ with respect to the number of ridge particles (or jet-(medium parton) collisions) is

$$P(N, \phi_s) = \frac{1}{N_{\text{bin}}} \int d\mathbf{b}_0 \frac{dN_{\text{bin}}}{d\mathbf{b}_0}(\mathbf{b}_0) \delta[N - N_k(\mathbf{b}_0, \phi_s)], \quad (90)$$

which leads to the desired normalization of the distribution $P(N, \phi_s)$,

$$\int dN P(N, \phi_s) = 1, \quad (91)$$

and the total number of binary nucleon-nucleon collisions

$$N_{\text{bin}} = \int d\mathbf{b}_0 \frac{dN_{\text{bin}}}{d\mathbf{b}_0}. \quad (92)$$

Thus, the number of ridge particle yield per trigger particle (or the number of jet-(medium parton) collisions per trigger) at an azimuthal angle ϕ_s , averaged over all source points of binary collisions at all \mathbf{b}_0 points, is

$$\bar{N}_k(\phi_s) = \int NP(N, \phi_s)e^{-\zeta N} dN \Big/ \int P(N, \phi_s)e^{-\zeta N} dN. \quad (93)$$

In practical calculations, it is convenient to discretize N by replacing the delta function in Eq. (90) as

$$\delta(N - N_k) \rightarrow \{\Theta[N_k - (N - \Delta N/2)] - \Theta[N_k - (N + \Delta N/2)]\}/\Delta N. \quad (94)$$

Upon choosing $\Delta N = 1$, the normalization condition (91) becomes

$$\sum_{N=0}^{N_{\text{max}}} P(N, \phi_s) = 1, \quad (95)$$

as in our previous definition with the ϕ_s dependence now explicitly written out. Equation (90) in the discretized form of N becomes

$$P(N, \phi_s) = \frac{1}{N_{\text{bin}}} \int d\mathbf{b}_0 \frac{dN_{\text{bin}}}{d\mathbf{b}_0}(\mathbf{b}_0) \{\Theta[(N - \Delta N/2) - N_k(\mathbf{b}_0, \phi_s)] - \Theta[(N + \Delta N/2) - N_k(\mathbf{b}_0, \phi_s)]\}/\Delta N. \quad (96)$$

This equation facilitates the evaluation of $P(N, \phi_s)$. For a given ϕ_s , we evaluate $N_k(\mathbf{b}_0, \phi_s)$ at different source points \mathbf{b}_0 , place the quantity $dN_{\text{bin}}/d\mathbf{b}_0$ at the appropriate $[N - \Delta N/2 \leq N_k(\mathbf{b}_0, \phi_s) \leq N + \Delta N/2]$ bin, and accumulate the contributions from all jet source points at all \mathbf{b}_0 . The accumulated distribution, divided by $N_{\text{bin}}\Delta N$ is then the distribution function $P(N, \phi_s)$. For these calculations, we need the transverse densities of the binary nucleon-nucleon collisions and participant numbers. The transverse density of binary nucleon-nucleon collisions in Eq. (96) can be obtained from the Glauber model to be

$$\frac{dN_{\text{bin}}}{d\mathbf{b}_0}(\mathbf{b}_0) = ABT(\mathbf{b}_{A0})T(\mathbf{b}_{B0})\sigma_{\text{in}}^{NN}, \quad (97)$$

where $\mathbf{b}_{A0} = \mathbf{b}_0 + \mathbf{b}/2$ and $\mathbf{b}_{B0} = \mathbf{b}_0 - \mathbf{b}/2$. The quantity σ_{in}^{NN} is the nucleon-nucleon inelastic cross section, which we can take to be 42 mb at $\sqrt{s_{NN}} = 200$ [78]. The participant number transverse density needed in Eqs. (79) and (88) along the jet trajectory can be similarly obtained from the Glauber model to be

$$\frac{dN_{\text{part}}}{d\mathbf{b}'}(\mathbf{b}') = AT(\mathbf{b}'_A) + BT(\mathbf{b}'_B), \quad (98)$$

where the transverse coordinates are given by $\mathbf{b}'_A = \mathbf{b}' + \mathbf{b}/2$, and $\mathbf{b}'_B = \mathbf{b}' - \mathbf{b}/2$. These relations allows us to use Eq. (96) to evaluate $P(N, \phi_s)$. The distribution $P(N, \phi_s)$ can then be used in Eq. (75) to evaluate $R_{AA}(\phi_s)$, and in Eq. (76) or (93) to evaluate $\bar{N}_k(\phi_s)$. After $\bar{N}_k(\phi_s)$ and $R_{AA}(\phi_s)$ have been evaluated, we can average over all azimuthal angles ϕ_s and we obtain the ridge particles [or jet-(medium parton) collision] per trigger

$$\langle N_k \rangle = \int_0^{\pi/2} d\phi_s \bar{N}_k(\phi_s)/(\pi/2), \quad (99)$$

and

$$\langle R_{AA} \rangle = \int_0^{\pi/2} d\phi_s R_{AA}(\phi_s)/(\pi/2), \quad (100)$$

which is usually expressed just as R_{AA} .

Eq. (15) separates the ridge particle distribution into a geometry-dependent part, $\langle f_R \rangle (2/3) \langle N_k \rangle$, and the normalized ridge momentum distribution, $dF/d\mathbf{p}$. From the magnitude of the ridge yield, we have extracted phenomenologically in Section VI the values of $\langle f_R \rangle \langle N_k \rangle = 3.8$ for central AuAu collisions at $\sqrt{s_{NN}} = 200$ GeV. Ridge particles after production are attenuated before reaching the detector. It is reasonable to take the average ridge particle attenuation factor $\langle f_R \rangle$ to be the same as the average attenuation factor for jet component particles, $f_J = 0.632$, as both types of particles come out from the interacting region. We then get an estimate of $\langle N \rangle = \langle N_k \rangle = 6.0$ as the total number of kicked partons per trigger for the most-central AuAu collisions at 200 GeV. For numerical purposes, we shall use these average numbers as references, keeping in mind however that they depend on the attenuation factor $\langle f_R \rangle$ that may be uncertain.

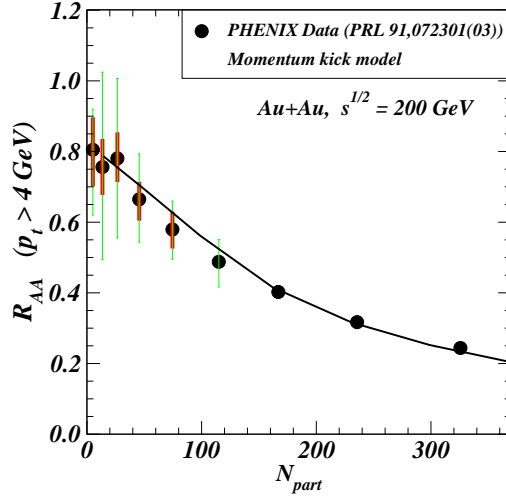


FIG. 8: (Color online) The ratio R_{AA} of the high- p_t π^0 trigger yield in AA collision, as a function of the number of participants N_{part} . The solid curve is the theoretical result from the momentum kick model, using $\zeta = 0.20$ and $\sigma = 0.7$ mb. The data points are from PHENIX high- p_t π^0 measurements for AuAu collisions at $\sqrt{s_{NN}} = 200$ GeV [79].

XIII. COMPARISON OF RIDGE YIELD WITH EXPERIMENTAL CENTRALITY DEPENDENCE

For a given impact parameter and azimuthal angle ϕ_s , the unknown parameters are ζ , and σ . Although all quantities depend on these two parameters, the quantity R_{AA} for the quenching of the trigger is more sensitive to ζ , and the ridge yield per trigger is more sensitive to σ . We find that the totality of experimental data of the centrality dependence of R_{AA} and the centrality dependence of the ridge yield, can be explained well when we use

$$\zeta = 0.20, \text{ and } \sigma = 1.4 \text{ mb.} \quad (101)$$

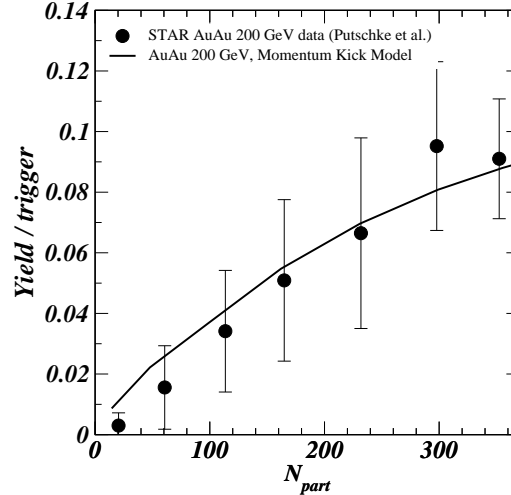


FIG. 9: (Color online) The ridge yield per trigger as a function of the participant number N_{part} for nucleus-nucleus collisions at $\sqrt{s_{NN}}=200$ GeV. The solid curve gives the theoretical result for AuAu collisions in the momentum kick model. The solid circular data points are from the STAR Collaboration [7].

We discuss here the comparison of theoretical results with experimental data using the above two parameters for AuAu collisions at $\sqrt{s_{NN}}=200$ GeV. Solid circular points in Fig. 8 give experimental PHENIX R_{AA} data for high- p_t π^0 yields [79]. Theoretical R_{AA} result in the momentum kick model obtained with Eq. (75) as a function of the participant number is shown as the solid curve. It gives good agreement with experimental R_{AA} data. The quenching of the jet is well accounted for in the momentum kick model.

The STAR AuAu ridge yield per trigger at $\sqrt{s_{NN}}=200$ GeV, shown as solid circular points in Fig. 9, are taken from Fig. 2 of [7]. They were obtained for $3 < p_{t,\text{trig}} < 4$ GeV and $2.0 < p_{t,\text{associated}} < p_{t,\text{trig}}$. The solid curve in Fig. 9 is the theoretical ridge yield per trigger for AuAu collisions. It has been normalized to match the data point (within errors) for the most-central collision examined in Sections IV-VI. Our comparison of momentum kick model results and the experimental data in Fig. 9 indicates that theoretical ridge yields per trigger agree with experiment. It increases as the number of participants increases.

The value of $\zeta = 0.20$ is nearly the same as our earlier estimate of $\zeta = 0.22$ arising from collisional jet momentum loss alone. This indicates that collisional momentum loss may contribute the dominant component of the jet momentum loss, but more research on theoretical predictions for ζ are needed to separate out the different absorptive and radiative contributions. The cross section corresponds to a parton interacting radius of 0.21 fm, which means that a parton having the entropy content of a hadron appears to the jet probe as a strongly interacting scattering disk with a radius of 0.21 fm.

XIV. DEPENDENCE OF THE RIDGE YIELD ON COLLIDING NUCLEI MASSES AND ENERGIES

Whereas our attention so far has been focused on AuAu collisions at $\sqrt{s_{NN}} = 200$ GeV, we would like to investigate in this section how the ridge yield scales with the mass numbers and the energies of the colliding nuclei. Experimental data for such an analysis have been obtained by the STAR Collaboration with the acceptance region of $3 < p_{t,\text{trig}} < 4$ GeV and $2.0 < p_{t,\text{associated}} < p_{t,\text{trig}}$ [8, 14]. This region of acceptance is slightly different from the acceptance region for Fig. 9 used in Ref. [7]. The measurements of the ridge yield for AuAu and CuCu collisions at $\sqrt{s_{NN}}=200$ and 62 GeV within the same acceptance region in [8, 14] allows a consistent comparison across mass numbers and energies of the colliding nuclei. The experimental ridge yield as a function of the participant numbers are shown in Fig. 10 as solid points for AuAu collisions and open points for CuCu collisions [8, 14]. The circular data points are for $\sqrt{s_{NN}} = 200$ GeV and the square points are for 62 GeV. One notes that the ridge yield appears to increase with increasing number of participants and increasing collision energies. The ridge yield for CuCu collisions is small and contains large systematic errors.

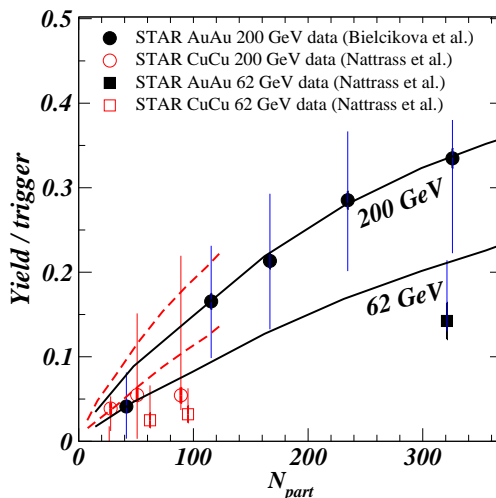


FIG. 10: (Color online) The ridge yield per trigger as a function of the participant number N_{part} for nucleus-nucleus collisions at $\sqrt{s_{NN}}=200$ and 62 GeV. The solid curves are theoretical results for AuAu collisions and the dashed curves for CuCu collisions in the momentum kick model. The solid points represent AuAu data and the open points represent CuCu data, from the STAR Collaboration [8, 14].

We show in Fig. 10 the theoretical ridge yield for AuAu and CuCu collisions as a function of the number of participants for $\sqrt{s_{NN}} = 200$ and 62 GeV. The experimental and theoretical ridge yields are matched for the most-central AuAu collision data point at $\sqrt{s_{NN}} = 200$ GeV. Our comparison of momentum kick model results and the experimental data at different energies, different nuclear masses, and different participant numbers indicates that the theoretical ridge yield agrees well with experiment. For the same nucleus-nucleus collision at different energies, the theoretical ridge yield scales approximately with κ , the number of medium partons produced per participant, which increases with increasing collision energy as $(\ln \sqrt{s})^2$ [76]. For the same collision energy, the theoretical ridge yields per trigger for CuCu collisions follow approximately those of the ridge yields for AuAu collisions, when plotted in

terms of the number of participants.

XV. DISCUSSIONS AND CONCLUSIONS

The experimental near-side ridge data have guided us to the momentum kick model as a description of the ridge phenomenon. The narrow cone of associated particles along the jet direction reveals that the trigger particle is connected with the occurrence of a jet. The yield of the associated particles as increasing with increasing participant numbers and the similarity of their inverse slope reveal that the ridge particles come from medium particles. The short-range behavior of the strong interaction due to color screening and the narrow azimuthal correlation of a ridge particle with the trigger particle reveal further that the ridge particles and the jet are related by collisions. Hence, a picture of the momentum kick model emerges as a plausible description of the ridge phenomenon.

In the momentum kick model, a jet parton produced in high-energy heavy-ion collisions makes collisions with medium partons. The kicked medium partons subsequently materialize as ridge particles while the jet loses energies and fragments into the trigger particle and other fragmentation products.

The implementation of the momentum kick model can proceed numerically by a Monte Carlo approach, following the trajectory of the jet and the medium particles as the medium evolves. The space-time dynamics of the medium and the jet is a problem of great complexity and contains many complex, unknown, and non-perturbative elements. However, before we implement such an elaborate undertaking, it is useful to explore with simplifying assumptions whether the momentum kick model contains promising degrees of freedom.

Following the dynamics of a jet and its interaction with the medium, we show how the ridge yield can be greatly simplified by using the average distribution of the medium particles and the average momentum kick. We are then able to separate the ridge particle yield into a factor which depends on the average number of partons kicked by the jet and another factor related to the (average) momentum distribution of the kicked parton after acquiring a momentum kick from the jet. The ridge particles therefore carries information on the momentum distribution of the partons at the moment of jet-(medium parton) collisions. They also carry information on the (average) magnitude of the momentum kick a medium parton acquires. These complications of space-time dynamics of medium and jet partons have been subsumed under the probability distribution $P_N(N)$, which depends on geometry, medium parton dynamics, jet parton trajectories, and jet-(medium parton) cross sections.

The medium partons kicked by the jet materialize as ridge particles can be used to extract the early parton momentum distribution. The extracted early parton momentum distribution provides valuable information for the mechanism of early parton production and the later evolution of the system toward the state of quark-gluon plasma. For central AuAu collision at $\sqrt{s_{NN}} = 200$ GeV, we find the extracted early parton momentum distribution to have a thermal-like transverse distribution but a rapidity plateau structure whose width decreases as the transverse momentum increases. We should note that plateau rapidity structure has been known in QCD particle production experiments [36, 37, 38, 39, 40] and in QCD particle production theories [42, 43, 44, 45, 46]. From this viewpoint, the occurrence of a plateau structure at the early stage of nucleus-nucleus collision should not come as a surprise.

The rapidity plateau distribution differs from the rapidity distribution of the bulk matter which is found to have a Gaussian shape [65, 66, 67]. It is important to note that jets occur at an early stage of the nucleus-nucleus collisions, whereas the bulk medium properties are measured at the end-point of the nucleus-nucleus collision. A significant dynamical evolution must have occurred between the early beginning of the nucleus-nucleus collision and the end-point of the nucleus-nucleus collision. Therefore the early parton momentum distribution near the beginning stage of the nucleus-nucleus collision needs not be the same as the bulk matter distribution at the end-point of the nucleus-nucleus collision. One expects that starting with a non-isotropic plateau rapidity distribution that is much elongated in the longitudinal direction, a collision of two partons with large and opposing longitudinal momenta in adjacent spatial locations will redistribute the partons from the longitudinal direction towards the transverse directions, with a decrease in the longitudinal momenta of the colliding partons. Hence, the evolution will likely smooth out the anisotropic plateau rapidity structure to a significant degree as time proceeds.

The subject of our focus being the near-side ridge and jet quenching in the early collision history, how the parton distribution function $F(\mathbf{r}, \mathbf{p}, t)$ evolves subsequently from the initial state to the end-point of nucleus-nucleus collision is beyond the scope of the present manuscript. The complete problem of parton evolution is a problem of great complexity [30, 31, 56, 80, 81, 82, 83], involving perturbative and non-perturbative elements. For example, in one of the descriptions using the Color-Glass-Condensate treatment of the initial conditions [31], it is not well-understood even within the Color-Glass-Condensate community how the initial large rapidity correlations can evolve into to a thermal distribution in a short period of time of 1-2 fm/c or to a Gaussian rapidity distribution at the end-point of the nucleus-nucleus collision. Some recent advances suggest intrinsic color plasma instabilities that can lead to a breaking of the boost invariance [30, 80, 81], and other investigations suggest the bottom-up scenario involving $gg \rightarrow ggg$ [82, 83]. The extracted early momentum distribution of a rapidity plateau obtained here serves to high-light the

important and unsolved issues of parton evolution that are left outstanding by the present findings of this manuscript.

The momentum loss of the jet parton and the geometry of the jet trajectory are other important aspects of the momentum kick model. The magnitude of the momentum kick imparted onto the medium parton has been found to be $q = 1.0$ GeV per jet-(medium parton) collision. This momentum gain by the kicked parton is clearly related to the momentum loss of the jet as a result of the jet-(medium parton) collisions. One obtains a good phenomenological description of the experimental data of the centrality dependence and collisional energy dependence of R_{AA} and the ridge yield. The extracted physical quantities furnish important, albeit approximate, empirical data for future investigations on the dynamics of parton production, parton evolution, and jet energy loss. The subject will come over and over again, each time with more and more accuracy and refinement, as we go through our course in physics.

The successes of the simplifying model indicates that the momentum kick model contains promising degrees of freedom for the description of the gross features of the ridge phenomenon and jet quenching. There is however a limited range for the application of a completely analytical formulation, as many refinements and improvements necessitate additional degrees of freedom. Among other things, we envisage the need for a better description of the elementary jet-(medium parton) collision process, a better description of the dynamics of the medium, and the inclusion of effects of medium transverse collective and elliptic flows that depend on the reaction plane orientations and medium spatial locations. There is the further complication for intermediate p_t trigger particles that some of the trigger particles may arise not from the jets but from the medium [33]. A Monte Carlo implementation of the momentum kick model that will allow the inclusion of many refinements and improvements, and will therefore be of great interest.

The author wishes to thank Drs. Fuqiang Wang, V. Cianciolo, Jianguyong Jia, Zhangbu Xu, and C. Nattrass for helpful discussions and communications. This research was supported in part by the Division of Nuclear Physics, U.S. Department of Energy, under Contract No. DE-AC05-00OR22725, managed by UT-Battelle, LLC.

-
- [1] K. Adcox *et al.*, PHENIX Collaboration, Nucl. Phys. **A757**, 184 (2005).
 - [2] J. Adams *et al.*, STAR Collaboration, Nucl. Phys. **A757** 102 (2005).
 - [3] I. Arsene *et al.*, BRAHMS Collaboration, Nucl. Phys. **A757**, 1 (2005).
 - [4] B. B. Back *et al.*, PHOBOS Collaboration, Nucl. Phys. **A757**, 28 (2005).
 - [5] J. Adams *et al.* for the STAR Collaboration, Phys. Rev. Lett. **95**, 152301 (2005).
 - [6] J. Adams *et al.* (STAR Collaboration), Phys. Rev. C **73**, 064907 (2006).
 - [7] J. Putschke (STAR Collaboration), J. Phys. **G74**, S679 (2007), arXiv:nucl-ex/0701074.
 - [8] J. Bielcikova (STAR Collaboration), J. Phys. **G74**, S929 (2007), arXiv:nucl-ex/0701047.
 - [9] F. Wang (STAR Collaboration), Invited talk at the XIth International Workshop on Correlation and Fluctuation in Multiparticle Production, Hangzhou, China, November 2007, [arXiv:0707.0815].
 - [10] J. Bielcikova for the STAR Collaboration, Talk presented at 23rd Winter Workshop on Nuclear Dynamics, Big Sky, Montana, USA, February 11-18, 2007, [arXiv:0707.3100]; J. Bielcikova for the STAR Collaboration, Talk presented at XLIII Rencontres de Moriond, QCD and High Energy Interactions, La Thuile, March 8-15, 2008, [arXiv:0806.2261];
 - [11] B. Abelev (STAR Collaboration), Talk presented at 23rd Winter Workshop on Nuclear Dynamics, Big Sky, Montana, USA, February 11-18, 2007, [arXiv:0705.3371].
 - [12] L. Molnar (STAR Collaboration), [nucl-ex/0701061].
 - [13] J. Longacre (STAR Collaboration), Poster presented at presented at the 19th International Conference on Ultra-Relativistic Nucleus-Nucleus Collisions, "Quark Matter 2006", Shanghai, China, November 14-20, 2006, [nucl-ex/0702008].
 - [14] C. Nattrass (STAR Collaboration), J. Phys. G **35**, 104110 (2008).
 - [15] P. K. Netrakanti (STAR Collaboration), J. Phys. G **35**, 104010 (2008).
 - [16] A. Adare *et al.*, PHENIX Collaboration, Phys. Rev. C **78**, 014901 (2008).
 - [17] M. P. McCumber, PHENIX Collaboration, J. Phys. G **35**, 104081 (2008).
 - [18] E. Wenger (PHOBOS Collaboration), J. Phys. G **35**, 104080 (2008),
 - [19] C. Y. Wong, Phys. Rev. C **76**, 054908 (2007).
 - [20] C. Y. Wong, Chin. Phys. Lett. **25**, 3936 (2008).
 - [21] C. Y. Wong, J. Phys. G **35**, 104085 (2008),
 - [22] R. C. Hwa and C. B. Yang, Phys. Rev. C **67** 034902 (2003); R. C. Hwa and Z. G. Tan, Phys. Rev. C **72**, 057902 (2005); R. C. Hwa and C. B. Yang, [nucl-th/0602024].
 - [23] C. B. Chiu and R. C. Hwa Phys. Rev. C **72**, 034903 (2005).
 - [24] R. C. Hwa, [arXiv:0708.1508].
 - [25] P. Romatschke, Phys. Rev. C **75** 014901 (2007).
 - [26] S. A. Voloshin, Nucl. Phys. **A749**, 287 (2005).
 - [27] N. Armesto, C. A. Salgado, U. A. Wiedemann, Phys. Rev. Lett. **93**, 242301 (2004).
 - [28] E. Shuryak, Phys. Rec. C **76**, 047901 (2007).
 - [29] V. S. Pantuev, [arXiv:0710.1882]

- [30] A. Dumitru, Y. Nara, B. Schenke, and M. Strickland, Phys. Rev. C **78**, 024909 (2008).
- [31] A. Dumitru, F. Gelis, L. McLerran, and R. Venugopalan, Nucl. Phys. **A810**, 91 (2008).
- [32] R. Mizukawa, T. Hirano, M. Isse, Y. Nara, and A. Ohnishi, J. Phys. G **35**, 104083 (2008).
- [33] Jianyong Jia and R.. Lacey, [arXiv:0806.1225].
- [34] S. Gavin, and G. Moschelli, J. Phys. G **35**, 104084 (2008).
- [35] S. Gavin, L. McLerran, and G. Moschelli, [arXiv:0806.4718].
- [36] H. Aihara *et al.* (TPC/Two-Gamma Collaboration), Lawrence Berkeley Laboratory Report LBL-23737 (1988).
- [37] W. Hofmann, Ann. Rev. Nucl. Sci. **38**, 279 (1988).
- [38] A. Petersen *et al.* (Mark II Collaboration), Phys. Rev. D **37**, 1 (1988).
- [39] K. Abe *et al.* (SLD Collaboration), Phys. Rev. D **59**, 052001 (1999).
- [40] K. Abreu *et al.* (DELPHI Collaboration), Phys. Lett. B **459**, 397 (1999).
- [41] Note that the rapidity distributions along the sphericity axis and the thrust axis are nearly the same on almost all rapidity points except at $|y| \lesssim 0.1$ (see Figs. 40 and 41 in Ref. [36]). While the rapidity distribution obtained in the sphericity axis system appears to be smooth around $y \sim 0$, the rapidity distribution obtained in the thrust axis system exhibits an abrupt decrease at $|y| \lesssim 0.1$.
- [42] A. Casher, J. Kogut, and L. Susskind, Phys. Rev. D **10**, 732 (1974)
- [43] J. D. Bjorken, Phys. Rev **D27**, 140 (1983).
- [44] C. Y. Wong, R. C. Wang, and C. C. Shih, Phys. Rev. D **44**, 257 (1991).
- [45] C. Y. Wong, *Introduction to High-Energy Heavy-Ion Collisions*, World Scientific Publisher, 1994.
- [46] B. Andersson, G. Gustafson, G. Ingelman, and T. Sjöstrand, Phys. Rep. **97**, 31 (1983); T. Sjöstrand, Comp. Phys. Comm. **39**, 347 (1986); T. Sjöstrand and M. Bengtsson, Comp. Phys. Comm. **43**, 367 (1986); B. Andersson, G. Gustafson, and B. Nilsson-Alqvist, Nucl. Phys. **B281**, 289 (1987).
- [47] J. Schwinger, Phys. Rev. **128**, 2425 (1962); J. Schwinger, in *Theoretical Physics*, Trieste Lectures, 1962 (I.A.E.A., Vienna, 1963), p. 89.
- [48] J. H. Lowenstein and J. A. Swieca, Ann. Phys. (N.Y.) **68**, 172 (1971).
- [49] S. Coleman, R. Jackiw, and L. Susskind, Ann. Phys. **93**, 267 (1975).
- [50] S. Coleman, Ann. Phys. **101**, 239 (1976).
- [51] J. Casalderrey-Solana, and C. A. Salgado, [arXiv:0712.3443]; S. Wicks and M. Gyulassy, J. Phys. G**34**, S989 (2007); M. Gyulassy, P. Levai, and I. Vitev, Nucl. Phys. **B 594**, 371 (2001); S. Wicks, S. Horowitz, W. Djordjevic, and M. Gyulassy, Nucl. Phys. A **784**, 426 (2007); I. Vitev, Phys.Lett. **B639**, 38 (2006); E. Wang and X. N. Wang, Phys. Rev. Lett. **87**, 142301 (2001); E. Wang and X. N. Wang, Phys. Rev. Lett. **89**, 162301 (2002); A. Drees, H. Feng, and J. Y. Jia Phys. Rev. **C71**, 034909 (2005).
- [52] O. Kaczmarek and F. Zantow, Phys. Rev. D **71**, 114510 (2005).
- [53] C. Y. Wong, Phys. Rev. C **65**, 034902 (2002); C. Y. Wong, Phys. Rev. C **65**, 014903 (2002); C. Y. Wong, J. Phys. G **28**, 2349 (2002); C. Y. Wong, Phys. Rev. C **72**, 034906 (2005). C. Y. Wong, Talk presented at Recontre de Blois, Chateau de Blois, France, May 15-20, 2005 [arXiv:hep-ph/0509088]; C. Y. Wong, Phys. Rev. C **76**, 014902 (2007); C. Y. Wong, J. Phys. G **32**, S301 (2006).
- [54] M. Mostafa and C. Y. Wong, Phys. Rev. C **51**, 2135 (1995).
- [55] C. Y. Wong, Phys. Rev. C **48**, 902 (1993)
- [56] B. A. Li, and C. M. Ko, Phys. Rev. C **54**, 3283 (1996); X. N. Wang and M. Gyulassy, Comp. Phys. Comm. **83**, 307 (1994); N. Armesto and C. Pajares, Int. J. Mod. Physi **A15**, 2019 (2000) [hep-ph/0002163]; S. Joelan and J. Kapusta, "LEXUS", Phys. Rev. C **56**, 468 (1997); C. Y. Wong, and Z. D. Lu, Phys. Rev. D **39**, 2606 (1989); B. Andersson, G. Gustafson, and B. Nilsson-Alqvist, Nucl. Phys. **B281**, 289 (1987); A. Cappella and J. Tran Thanh Van, Zeit. Phys. C **38**, 177 (1988); K. Werner, Phys. Rev. D **39**, 780 (1988); H. Sorge, H. Stöcker, and W. Greiner, Nucl. Phys. **A498**, 567c (1989); K. Geiger and B. Müller, Nucl. Phys. **A544**, 467c (1992); L McLerran, [arXiv:0804.1736]; A. Dumitru, F. Gelis, L. McLerran, and R. Venugopalan, Nucl. Phys. **A810**, 91 (2008).
- [57] T. Fujita and J. Hüfner, Phys. Rev. D **40**, 604, (1989).
- [58] R. D. Field and R. P. Feynman, Phys. Rev. D **15**, 2590 (1977).
- [59] H. Verlinde and E. Verlinde, [hep-th/9302104].
- [60] R. C. Wang and C. Y. Wong, Phys. Rev. D **38**, 348 (1988).
- [61] H. P. Pavel and D. M. Brink, Z. Phys. C **51**, 119 (1991).
- [62] G. Gatoff, and C. Y. Wong, Phys. Rev. D **46**, 997 (1992).
- [63] C. Y. Wong, R. C. Wang, and J. S. Wu, Phys. Rev. D **51**, 3940 (1995).
- [64] C. Adam, Phys. Lett. **B555**, 132 (2003).
- [65] M. Murray for the Brahm's Collaboration, J. Phys. G. **30**, S667 (2004)
- [66] P. Steinberg, Nucl. Phys. **A752**, 423 (2005).
- [67] P. Steinberg, Proceedings of 3rd International Workshop on Critical Point and Onset of Deconfinement, Florence, Italy, 3-6 Jul 2006. arXiv:nucl-ex/0702019.
- [68] J. F. Owen, E. Reya, and M. Glück, Phys. Rev. D **18**, 1501 (1978).
- [69] D. J. Gross, Phys. Rev. Lett. **32**, 1071 (1974).
- [70] U. W. Heinz and P. F. Kolb, Nucl. Phys. **A702**, 269 (2002).
- [71] L. D. Landau, Izv. Akad. Nauk SSSR **17**, 51 (1953).
- [72] S. Z. Belenkij and L. D. Landau, Usp. Fiz. Nauk **56**, 309 (1955); Nuovo Cimento, Suppl. **3**, 15 (1956).
- [73] C. Y. Wong, Phys. Rev. C **78**, 054902 (2008).

- [74] C. Y. Wong, [arXiv:0809.0517].
- [75] G. Baym, B. L. Friman, J.-P. Blaizot, M. Soyeur, and W. Czyz, Nucl. Phys. **A407**, 541 (1983).
- [76] W. Busza, Acta. Phys. Polo. **B35**, 2873 (2004), nucl-ex/0410035.
- [77] B. B. Back *et al.* (PHOBOS Collaboration), Nucl. Phys. **A 757**, 28 (2005).
- [78] C. Caso *et al.* (Particle Data Grup), Eur. Phys. J. C **3**, 1 (1998).
- [79] J. Adams *et al.* (PHENIX Collaboration), Phys. Rev. Lett. **91**, 172301 (2003).
- [80] S. Mrowczynski, Phys. Lett. B **314**, 118 (1993); [arXiv:0810.1515].
- [81] A. Rebhan, P. Romatschke, and M. Strickland, Phys. Rev. Lett. **94**, 102303 (2005).
- [82] Z. Xu, C. Greiner, and H. Stoecker, [arXiv:0807.2986]; A. El, Z. Xu, and C. Greiner, Nucl. Phys. A **806**, 287 (2008).
- [83] A. H. Mueller, Nucl. Phys. B **572**, 227 (2000).